Mesoscale crystal plasticity modeling of nanoscale Al-Al_2Cu eutectic alloy

Guisen Liu[a], Dongyue Xie[a], Shujuan Wang[b], Amit Misra[b], Jian Wang[a,*]

[a] Mechanical and Materials Engineering, University of Nebraska-Lincoln, Lincoln, NE 68588, USA.

[b] Department of Materials Science and Engineering, College of Engineering, University of Michigan, Ann Arbor, MI 48109-2136, USA.

Abstract

Nanolaminated composites composed of alternate metal and intermetallic or ceramic lamellae exhibit high strength, high strain hardening rate and measurable plasticity at ambient and elevated temperatures. Due to the difference in plastic deformation capability between the two phases, structural instability occurs in hard lamellae associated with buckling when a compression strain is applied parallel to the lamellae. Taking nanoscale Al-Al_2Cu eutectic alloy as a model system, we develop a mesoscale crystal plasticity (CP) model based on the confined layer slip (CLS) mechanism (referred to as CLS-CP) to understand the buckling behavior of the nanolaminates. In the CLS-CP model, buckling in Al_2Cu lamellae is constrained by the elastic-plastic deformation of Al lamellae. The critical resolved shear stress for dislocation slip in Al lamellae varies with layer thickness, estimated by the CLS mechanism. To capture the essential features of confined layer slip mechanism that dislocations propagate within the layer and are deposited at the interfaces, plastic deformation in each lamella is the same through the layer thickness. The variation of elastic deformation through the layer thickness is captured through dividing each Al lamella into three or more elements that have the same plastic deformation through the thickness. In comparison, we also conduct standard crystal plasticity modeling in which plastic deformation in the three elements through the layer thickness is calculated individually according to phenomenological power law. In these simulations, plasticity in Al_2Cu lamellae is modeled with slips on {121} planes due to the slip continuity across the interface, which have been observed in our recent experiments. The CLS-CP model is able to predict mechanical properties of nano-scale lamellar materials. In contrast, the standard CP model is more suitable to study deformation behavior of sub-micro scale lamellar materials. The CLS-CP model calculations reveal that critical compression strain corresponding to buckling increases as layer thickness decreases, which agree with micro-pillar compression tests.

* Corresponding author: Jian Wang (jianwang@unl.edu)

Key words: buckling, nanolaminates, Al-Al_2Cu eutectic alloy, crystal plasticity.

1. Introduction

Nanolaminated materials composed of alternate metal (soft) and intermetallic or ceramic (hard) phases have attracted intensive attention because of their high strength, high strain hardening rate and measurable plasticity at ambient and elevated temperatures (Bhattacharyya et al., 2010; Choudhuri et al., 2018; Lei et al., 2017; Li and Liu, 2018; Raghavan et al., 2015; Yang et al., 2016). The enhanced plasticity is ascribed to the geometric compatibility between adjacent layers, while the high strain hardening originates mainly from the incompatibility in plastic deformation between them (Wang and Misra, 2014; Wang et al., 2017). Plastic deformation commences in soft phase associated with the nucleation and gliding of dislocations. Hard lamellae act as strong barriers for the motion of dislocations in soft lamellae. As a result, the propagation of dislocations is confined in the lamellae, resulting in dislocation deposition and accumulation in the soft/hard phases interfaces. Particularly due to the geometric compatibility between adjacent lamellae, the hard phase elastically deforms to accommodate the elastic and plastic deformation in the soft phase. Consequently, strain hardening develops in the soft phase associated with back stress due to the plastic deformation incompatibility between adjacent lamellae, and high stress develops in the hard phase. The high stress may trigger uniformly or localized shear in hard phase (referred to as plastic co-deformation) or cracking in hard phase (referred to as failure). Cracks in hard phase initiate by the increased tensile stress due to loading transfer in tension test or bending induced tensile stress in compression test. These mechanical behaviors are strongly related to the plastic deformability and the layer thickness of the hard phase. Taking the Al-Cu eutectic alloy as an example, in as-cast samples with the layer thickness above 500 nm, tensile stress causes mode I cracking in hard Al_2Cu phase, and compressive stress causes buckling and eventually cracking in hard Al_2Cu phase. In laser re-melted samples with the layer thickness less than 150 nm, plastic co-deformation happens through localized shear on {101} and {121} planes in hard Al_2Cu phase, and even buckling occurs at large compression but no cracking (Wang et al., 2018b). Such buckling instability was widely observed in soft/hard laminated structures, such as Al/SiC laminated composites (Mayer et al., 2016a; Mayer et al., 2016b) and pearlitic steel (Kapp et al., 2016). Ultimately, the bending of hard phase causes crack initiation, as observed in Al-SiC (Chawla et al., 2008), pearlitic steel (Zhang et al., 2010), Al-TiN (Li et al., 2014) and Al-Al_2Cu (Wang et al., 2018b).

Extensive experimental and theoretical work on mechanical properties of laminated composites revealed the length-scale dependent deformation mechanisms (Dehm et al., 2018; Misra et al., 2005a). For layer thickness > ~100 nm, flow strength can be described by dislocation pile-up model (Anderson and Li, 1995; Friedman and Chrzan, 1998; Li and Liu, 1967), and the relation between flow strength σ_c and layer thickness h obeys the Hall-Petch law, $\sigma_c \propto h^{-1/2}$. As the layer thickness decreases to several tens of nanometers, flow strength can be estimated according to confined layer slip (CLS) mechanism (Anderson et al., 1999; Embury and Hirth, 1994; Misra et al., 2004). The slip resistance of the dislocation loop has the relation $\sigma_c \propto h^{-1}\ln(h)$ with layer thickness (Misra et al., 2005a). When the layer thickness is in the range of a few nanometers, flow strength becomes insensitive to the layer thickness, instead, largely dependent on the structures and properties of interfaces between the two phases (Clayton, 2018; Damadam et al., 2018; Mara et al., 2016; Shao et al., 2018b; Wang et al., 2014b; Wang et al., 2017). Interfaces act as barriers for motion of dislocations, strengthening materials (Wang et al., 2014b). Meanwhile, interfaces act as sources for nucleating interfacial dislocations (Wang et al., 2008b; Wang and Misra, 2011) and lattice dislocations (Beyerlein et al., 2013; Dodaran et al., 2019; Shao et al., 2015; Wang et al., 2012; Zhang et al., 2012), providing additional pathways of plastic deformation.

Numerical models at different scales have been employed and developed to understand and predict mechanical properties of laminated composites. Molecular static/dynamic (MS/MD) modeling at atomic scale made significant contribution to fundamental understanding of structures and properties of interfaces and interface-dominated deformation events (Kim et al., 2016; Liang et al., 2016; Liu et al., 2019; Lu et al., 2018; Maresca et al., 2018; Shao et al., 2018a; Shao and Wang, 2016; Wang et al., 2008a; Wang et al., 2014a; Zhou et al., 2016b), yet MD cannot predict real stress-strain response due to the intrinsic limitation of high strain rate (10^8 s^{-1}), small dimensions (hundreds of nanometers), and short simulation duration (nanoseconds). Dislocation dynamics (DD) simulations at micro-scale can simulate collective dislocation activities and dislocation-interface interactions (Burbery et al., 2017; Hodapp et al., 2018; Shao et al., 2018c), thus DD is capable of capturing the nucleation of lattice dislocations from interfaces, the glide of threading dislocations inside lamella, and the stress-strain curves (Cho et al., 2018; Huang et al., 2018; LeSar and Capolungo, 2018; Shao et al., 2018b; Wang et al., 2014b; Zeng et al., 2016). However, computational costs confined them to limited plastic strain

deformation and simulation size. Another challenge when using DD to simulate the deformation behavior in materials containing interface is the lack of well-established dislocation-interface interaction rules, which need to be carefully calibrated from high-fidelity experiments or fine-scale simulations (Shao et al., 2018b; Wang et al., 2014b). The calibration of those rules seems to be not trivial and needs to be conducted case by case when different materials system or material microstructures are concerned. These difficulties can be overcome by the dislocation-based continuum crystal plasticity (CP) modelling (Roters et al., 2010; Segurado et al., 2018), which is solved through either combination of mean-field approximations and the finite element methods, or by means of full-field simulation of the mechanical response of a representative volume element using either finite element method (FEM) (Albiez et al., 2019; Lin et al., 2016; Lu et al., 2019; Park et al., 2019; Yu et al., 2018; Zhang et al., 2018) or fast Fourier transform (FFT) method (Roters et al., 2019; Segurado et al., 2018). Moreover, slip transmission across interfaces has been taken care of by specializing elements at the interface affected zones (IAZ) in which the outcome of slip transmission is determined according to the Lee-Robertson-Birnbaum criterion (Lee et al., 1989; Mayeur et al., 2015). A slip continuity factor (Mayeur et al., 2015; Werner and Prantl, 1990) has been proposed to quantify the misorientation between the paired slips and further incorporated into the CP model to relate it to the slip resistance in the IAZ (Mayeur et al., 2015). However, these CP models are insufficient for simulating materials with nanoscale microstructure because the dominant deformation mechanisms change from dislocation activities in the bulk to interface-related dislocation activities. To investigate the size-dependent small-scale plasticity phenomena, the quantized CP model (Li et al., 2009), and the coupled discrete-continuum method have been proposed. Here the discrete could be either atomistic simulations (Xiong et al., 2012; Xu et al., 2017) or DD simulations (Cui et al., 2015; Zbib and Diaz de la Rubia, 2002), which will directly provide the material length-scale dependent dislocation interactions with interfaces and various defects. Another recent endeavor was made by Ardeljan et al (Ardeljan et al., 2018) when they predicted the anisotropy and hardening of Mg/Nb nanolayered composites using CP model. The variation of the slip resistance with the layer thickness was estimated according to the CLS mechanism. They meshed each single layer into multiple elements for 50 nm Mg/Nb multilayer and one element for 5 nm Mg/Nb multilayer. It is noticed that the mesh with multiple elements through one single layer ignores the fact that plastic deformation shall be the same through the layer thickness according to the CLS, while the mesh with one element through one single layer may underestimate the

heterogeneous elastic deformation through the layer thickness, especially for the bending deformation.

In this work, we develop a mesoscale CLS-based CP model (referred to as CLS-CP), which deals with the constant plastic deformation and the heterogeneous elastic deformation through the layer thickness. Taking Al-Al_2Cu eutectic alloy as a model system, which is composed of alternate face-centered cubic Al and body-centered tetragonal Al_2Cu lamellae with the well-defined orientation relationship (Wang et al., 2018a), we investigate buckling instability using our CLS-CP model. In contrast, we also simulate buckling behaviors of laminates using a standard CP model. The standard CP model predicts plastic deformation localized in the middle element of each Al layer while plastic deformation in the elements connected to interfaces is very small due to geometrical constraint imparted by the hard Al_2Cu layers, which is more like the deformation feature in sub-micron scale lamellar materials. Our CLS-CP model can well capture plastic deformation features occurring in nano-lamellar materials, i.e., homogeneous plastic deformation and heterogeneous elastic deformation through layer thickness, strain hardening in soft layers, and localized plastic deformation in hard layers. Furthermore, we discuss the effect of layer thickness and crystallographic anisotropy on the critical strength and strain as buckling occurs.

In what follows, we first describe CLS-CP model in section 2, followed by details in applying the model to simulate buckling under parallel compression in section 3. Then we validate the CLS-CP model through simulating buckling instability of nanoscale Al-Al_2Cu and comparing the CLS-CP predictions with the standard CP model, and further apply the CLS-CP model to study the effect of layer thickness and crystallographic anisotropy on buckling instability in section 4. We summarize the model and its applications in section 5.

2. Standard CP model and CLS-CP model

2.1. Fundamentals of standard CP model

Based on the kinematics of single crystal plasticity dated back to the works (Hill and Rice, 1972) and (Asaro, 1983), the total deformation gradient $\mathbf{F}$ at each material point can be decomposed into plastic deformation gradient $\mathbf{F_p}$ and an elastic deformation gradient $\mathbf{F_e}$,

$$\mathbf{F} = \mathbf{F_e}\mathbf{F_p} \tag{1}$$

$\mathbf{F_p}$ is a lattice reserving deformation to the plastic configuration; $\mathbf{F_e}$, which represents the elastic stretches and rigid body rotation, maps the plastic configuration into the deformed configuration. In the plastic configuration, the work conjugate Green-Lagrange strain $\mathbf{E_e}$ and second Piola-Kirchhoff stress tensor $\mathbf{S_p}$ are connected through the anisotropic elastic tensor $\mathbb{C}$,

$$\mathbf{S_p} = \mathbb{C}: \mathbf{E_e}, \quad \mathbf{E_e} = \frac{1}{2}\left(\mathbf{F_e^T F_e} - \mathbf{I}\right) \tag{2}$$

The second Piola-Kirchhoff stress in the plastic configuration $\mathbf{S_p}$ is related to the first Piola-Kirchhoff stress tensor in the reference configuration $\mathbf{P}$ through $\mathbf{P} = \mathbf{F_e S_p F_p^{-T}}$. From Eq. (1), the velocity gradient tensor $\mathbf{L}$ is decomposed as,

$$\mathbf{L} = \dot{\mathbf{F}}\mathbf{F}^{-1} = \dot{\mathbf{F}}_\mathbf{e}\mathbf{F}_\mathbf{e}^{-1} + \mathbf{F_e}\left(\dot{\mathbf{F}}_\mathbf{p}\mathbf{F}_\mathbf{p}^{-1}\right)\mathbf{F}_\mathbf{e}^{-1}, \text{ with } \mathbf{L_p} = \dot{\mathbf{F}}_\mathbf{p}\mathbf{F}_\mathbf{p}^{-1} \tag{3}$$

where the term in the parentheses is the plastic velocity gradient $\mathbf{L_p}$, which is mapped to the deformed configuration by $\mathbf{F_e}$. It is driven by $\mathbf{S_p}$ and depends on the internal state variables and microstructure, which can be parametrized in terms of dislocation slip rate $\dot{\gamma}^s$ and slip resistance g^s on each slip system s. For instance, the velocity gradient tensor $\mathbf{L_p}$, which is work conjugate with the Mandel stress $\mathbf{M_p}$ in the plastic configuration, can be formulated as the superposition of slip rates on all slip systems,

$$\mathbf{L_p} = \dot{\mathbf{F}}_\mathbf{p}\mathbf{F}_\mathbf{p}^{-1} = \sum_s \dot{\gamma}^s\, \mathbf{b^s} \otimes \mathbf{n^s} \tag{4}$$

with $\mathbf{b^s}$ and $\mathbf{n^s}$ being the unit vector along the slip direction and the normal of the slip plane of the s-th slip system respectively. For Al layers, there are twelve {111}<110> slip systems, i.e., s = 1, 2, …, 11, 12. Following the phenomenological crystal plasticity model proposed by Peirce et al (Peirce et al., 1982), the evolution of the slip rate $\dot{\gamma}^s$ is driven by the resolved shear stress τ^s under the slip resistance g^s,

$$\dot{\gamma}^s = \dot{\gamma}_0 \left|\frac{\tau^s}{g^s}\right|^{1/m} \mathrm{sgn}(\tau^s) \tag{5}$$

where $\dot{\gamma}_0$ is the reference strain rate on s-th slip system, m is the strain rate sensitivity of the slip. Within the framework of DAMASK (Roters et al., 2019; Shanthraj et al., 2018), the driving force for dislocation slip on the s-th slip system $\tau^s = \mathbf{M_p} \cdot \mathbf{b^s} \otimes \mathbf{n^s}$ is calculated from the Mandel stress, which is approximated by the second Piola-Kirchhoff stress tensor $\mathbf{S_p}$ under the assumption of $\mathbf{F_e^T F_e} \approx \boldsymbol{I}$ ($\boldsymbol{I}$ is second rank identity tensor). The slip resistance g^s represents the current strength of that slip system and its evolution reflects the strain hardening. For micro-thick Al, a simplified phenomenological power hardening law implemented in DAMASK (Shanthraj et al., 2018) is adopted, which is based on the dislocation interaction induced hardening (Asaro, 1983; Bassani

and Wu, 1991; Devincre et al., 2008; Tome et al., 1984). The slip resistance is assumed to increases asymptotically towards to a saturation resistance g_∞^s with increasing shear strain through the following relationship,

$$\dot{g}^s = H_0(1 - g^s/g_\infty^s)^w \sum_t h_{st}\dot{\gamma}^t \quad (6)$$

where fitting parameters H_0 and w are initial hardening slope and hardening exponent respectively, and h_{st} is the interaction hardening coefficient between s and t slip systems. We adopted constitutive parameters from the work of (Eisenlohr et al., 2013) in modeling bulk single crystal Al in our standard CP model. The initial critical resolved shear stress (CRSS, g_0^s) for dislocation in bulk single crystal Al is 31 MPa (Eisenlohr et al., 2013).

2.2. CLS-CP model

According to the CLS mechanism, plastic deformation is identical through the layer thickness while elastic deformation may vary through the layer thickness. Hereby, we mesh each layer with three elements through the layer thickness. The calculation details on plastic deformation in the three elements will be discussed later. To study the effect of the layer thickness (h) on mechanical response, the critical resolved shear stress of each slip system is a function of h according to the CLS mechanism. Localized plasticity in Al_2Cu layers is modeled based on paired slips according to the slip continuity across the Al/Al_2Cu interface. We implement our CLS-CP model into DAMASK (Düsseldorf Advanced Material Simulation Kit) (Roters et al., 2019) to study the mechanical response of Al-Al_2Cu eutectic alloy.

2.2.1 Layer thickness dependence of plastic flow

Corresponding to the confined layer slip mechanism, threading dislocations or loops nucleate from interfaces and propagate within the layer, and are ultimately deposited/accumulated on interfaces, as depicted in Fig. 1a. The initial critical resolved shear stress (CRSS, g_0^s) for a single confined layer slip event on the s-th slip system obeys the Orowan type relation (Anderson et al., 1999; Embury and Hirth, 1994),

$$g_0^s(b^s, h) = \tau_0 + \frac{c\mu b^s}{h^s}\ln(h^s/b^s) \quad (7)$$

The first term τ_0 is the lattice friction stress, independent on the layer thickness h or the interactions of dislocations with the interface. The second term is the resistance encountered by the dislocation as it propagates through the layer, where b^s is the Burgers vector of dislocation

gliding on s-th slip system, h^s is the distance on the slip plane between adjacent interfaces determined by the layer thickness h and the orientation of the slip plane, c is $1/(2\pi)$ for the screw dislocations and $1/(2\pi(1-\upsilon))$ for the edge dislocations, μ is shear modulus and υ is Poisson's ratio.

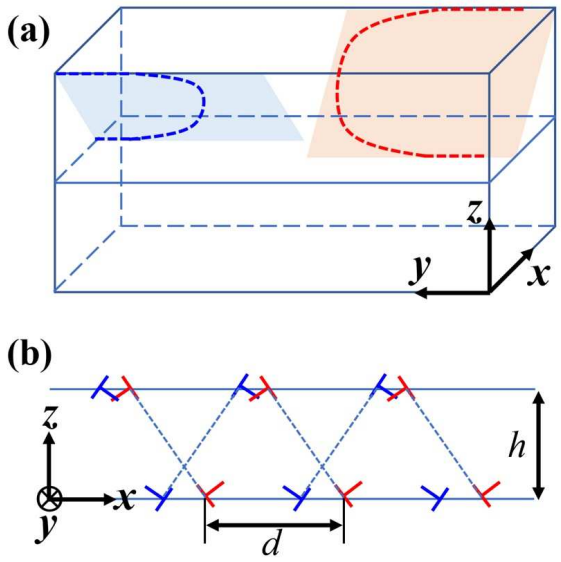

Fig. 1. Schematic illustration of confined layer slip mechanism in multilayers. (a) Propagation of two dislocations glide in one layer. (b) Uniform distribution of two groups of dislocations (blue and red) at the interface.

Corresponding to the CLS mechanism, the strain hardening originates from four aspects. First, the deposited dislocations at interfaces during deformation will resist gliding of dislocations that are parallel to the deposited dislocations (Anderson et al., 1999; Embury and Hirth, 1994). In this context, it is more favorable to deform a layer by single dislocation on numerous planes than multiple dislocations on fewer planes, resulting in periodic patterns of accumulated dislocations with spacing d. Fig. 1b illustrates the uniform distribution of net accumulated dislocations at interfaces. Second, the interface dislocations (both the deposited dislocations and misfit dislocations) nonparallel to the gliding loops will act as barriers for the gliding of dislocation loops, involving complex dislocation interactions. However, the effect is weak as demonstrated by dislocation dynamics simulations (Pant et al., 2003). Third, the hardening associated with interactions among gliding dislocations can be neglected because no dislocation cells form in nanolayers (Misra et al., 2005b). Fourth, back stress hardening originates from the incompatibility of plastic deformation between the metal layer and the brittle layer (Wang and Misra, 2014), which can be automatically taken into account in finite element

analysis. To understand the hardening effect resulted from parallel dislocations on interfaces, (Embury and Hirth, 1994) derived the critical CRSS for a single dislocation loop within a layer based on its interaction with the periodic deposited dislocation patterns,

$$g^s(b^s, h, d) = g_0^s + \frac{2c\mu b^s}{h^s} \ln\left(\frac{d}{2\pi b^s}\right) \tag{8}$$

(Anderson et al., 1999; Embury and Hirth, 1994) have shown that this hardening effect is weak in nano-laminates, because the net accumulated dislocations soon saturate when the layer thickness is on the nanometer scale. As a result, reducing the layer thickness will mainly increase $g_0^s(h)$ in Eq. (7) instead of the hardening in Eq. (8). Thus, the slip resistance was assumed to be the same as the initial CRSS $g_0^s(h)$ given by Eq. (7), that is $g^s \equiv g_0^s$. For simplicity, a factor k was used for the second term in Eq. (7) to scale the effect of layer thickness on the initial CRSS (Misra et al., 2005b),

$$g^s(b^s, h) \equiv g_0^s(b^s, h) = \tau_0 + k\frac{\mu b^s}{h} \ln\left(\frac{h}{b^s}\right) \tag{9}$$

In our models, τ_0 and k are used as fitting parameters, which will be determined in section 3.3. In the following section, we will describe the constant plastic deformation through the layer thickness corresponding to the confined layer slip mechanism.

2.2.2 Constant plastic deformation through layer thickness

Constant plastic deformation and heterogeneous elastic deformation through the layer thickness are realized in the CLS-CP model through meshing each lamella with three elements and enforcing the same plastic deformation in the three elements through the thickness. Fig. 2a illustrates a simulation model that comprises two bilayers with the equal layer thickness of h. The three elements through each layer are referred to as lower, middle and upper elements, denoted as i = 1, 2, 3 respectively. To achieve constant plastic deformation and different elastic deformation in one layer, the computation strategy is illustrated in Fig. 2b. Plastic deformation increment in the three elements is calculated based on the volume average stress, $\mathbf{S}_\mathbf{p}^a$, of stresses $\mathbf{S}_\mathbf{p}^i$ in the three elements.

$$\mathbf{S}_\mathbf{p}^a = \frac{1}{3}\left(\mathbf{S}_\mathbf{p}^1 + \mathbf{S}_\mathbf{p}^2 + \mathbf{S}_\mathbf{p}^3\right) \tag{10}$$

where $\mathbf{S}_\mathbf{p}^{i=1,2,3}$ is the second Piola-Kirchhoff stress tensor in the lower, middle and upper elements. When a nano-lamella is purely bent, the resolved shear stresses in the upper and lower elements have the opposite sign. If nucleation rate of dislocations was assumed to be equal and

these dislocations could glide through the layer, the net deformation is equal to zero due to their opposite sign. If the neutral plane does not lie in the middle of the lamella, plastic deformation will be generated due to the different magnitude of RSS in the upper and lower elements. Mathematically, the velocity gradient $\mathbf{L_p}$ in the middle element is firstly calculated by summing up the slip rate on each slip system in the middle element, which is determined by the average stress $\mathbf{S}_\mathbf{p}^a$, as specified in Eqs. (4-5). Then the plastic deformation gradient in the middle element $\mathbf{F}_\mathbf{p}^2$ is updated according to Eq. (2) by using the linearized backward Euler method (Roters et al., 2019). Following the flowchart of stress integration in Fig. 2b, updated elastic deformation gradient $\mathbf{F}_\mathbf{e}^{i=2}$ and second Piola-Kirchhoff stress $\mathbf{S}_\mathbf{p}^{i=2}$ in the middle element are obtained. They are iteratively solved using Newton-Raphson iteration method until the residuum $\mathbf{L_p}$ in the middle element is less than the preset tolerance 10^{-5}/s. At the same time, the velocity gradient $\mathbf{L_p}$ and plastic deformation gradient $\mathbf{F_p}$ in the middle element are assigned to the upper and lower elements in order to enforce the same plastic deformation in the three elements through the thickness,

$$\mathbf{L}_\mathbf{p}^{i=1} = \mathbf{L}_\mathbf{p}^{i=2}, \mathbf{L}_\mathbf{p}^{i=3} = \mathbf{L}_\mathbf{p}^{i=2};\ \mathbf{F}_\mathbf{p}^{i=1} = \mathbf{F}_\mathbf{p}^{i=2}, \mathbf{F}_\mathbf{p}^{i=3} = \mathbf{F}_\mathbf{p}^{i=2} \tag{11}$$

Then the elastic strain and stress of the lower and upper elements can be accordingly solved based

on Eqs. (1-4) as shown in the flowchart in Fig. 2b. By using the averaged stress tensor among the three elements through layer thickness direction to calculate the plastic deformation increment, the plastic deformation of one lamella is enforced to be the same through the thickness direction while elastic deformation accommodates the compatible deformation. In other words, any component of the plastic strain tensor in the three elements is the same.

Last, we want to emphasize that the method to mesh each nano-thick layer with three elements in this work is the first attempt to capture the heterogeneous elastic deformation through the layer thickness and ensure constant plastic deformation through the layer thickness. It is numerically least expensive but may still overestimate the elastic deformation due to interface constraint. This issue could be overcome by using more elements through one layer, or using more integration points for one element. Since Fourier-based spectral solver was used to solve the mechanical response in DAMASK, where each element is described by one integration point with its corresponding material parameters, we tested the strategy of using 5 elements

through one layer in the following section, which confirmed our hypothesis. More details and discussions will be described in the following sections.

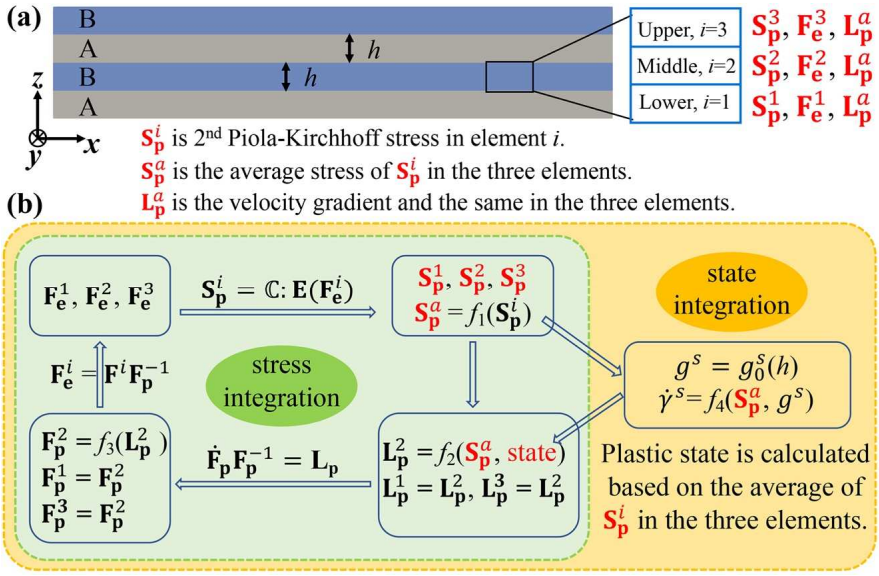

Fig. 2. (a) Illustration of a two bilayers model with equal thickness h for A and B layers. Each layer is meshed into three elements, referred to as lower, middle and upper elements and denoted as i = 1, 2 and 3 respectively. (b) Computation strategy for ensuring identical plastic deformation and heterogeneous elastic deformation through one lamella. For one layer composed of three elements (i = 1, 2 and 3), it includes a self-consistent inner-level integration of kinematic quantities at fixed internal plastic state, and an outer-level integration of internal material state using the average stress in the three elements.

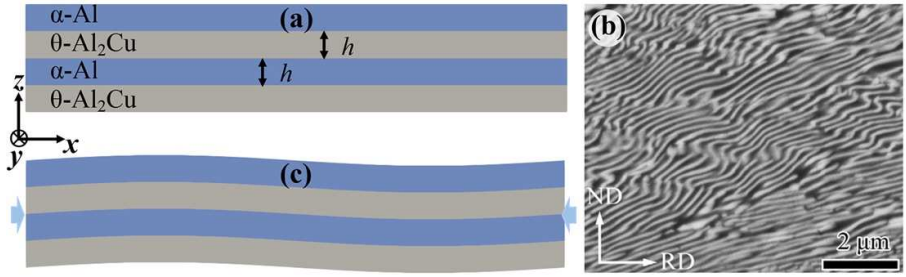

Fig. 3. (a, c) Illustration of a three dimensional periodic two bilayers Al-Al_2Cu lamellar structure model used in buckling simulation. (a) Initial configuration, and (c) Perturbated configuration after small amplitude sinusoidal perturbations applied to the initial geometry. Simple compression loading parallel to the lamellae (along x-axis) is applied to the perturbated configuration to simulate the buckling deformation of the layers. (b) Experimentally observed elastic bending of Al_2Cu lamellae in nanolayered Al-Al_2Cu after rolling parallel to lamellae, reproduced from (Wang et al., 2018b).

3. Models for buckling simulation

3.1 Buckling simulation

For the convenience of describing the model development, we start with the 3-element model. Fig. 3a shows the two bilayers model with the equal layer thickness of h, which will be used to simulate the buckling of Al_2Cu lamellae as observed in our recent experiments, Fig. 3b, (Wang et al., 2018b). Three-dimensional periodic boundary conditions were used corresponding to Fourier-based spectral method. For nanoscale Al-Al_2Cu eutectic alloy, the α-Al and θ-Al_2Cu layers hold the characteristic orientation relationship, $(001)_\alpha \| (001)_\theta$ and $[110]_\alpha \| [2\bar{1}0]_\theta$ (Wang et al., 2018a). The interface plane is $(001)_\alpha \| (001)_\theta$, whose plane normal direction is along the z-axis. The x-axis is along $[110]_\alpha \| [2\bar{1}0]_\theta$ and the y-axis is along $[\bar{1}10]_\alpha \| [120]_\theta$. To simulate the effect of layer thickness on buckling behavior, the geometry size of the model is intentionally designed to ensure the same bending stiffness for different h. In this study, the lengths along the x-, y- and z-directions vary with the layer thickness h, $L_x = 20h$, $L_y = h$ and $L_z = 4h$. The model is solved by discretizing this hexahedral cell with side lengths L_x, L_y and L_z into a regular grid of 240 × 4 × 12 = 8640 points. The solution field is approximated in the discrete Fourier space associated with this real space grid using Fast Fourier Transform method. Corresponding to this discretized 3-element model, there are totally 8640 C3D8R elements used in the simulations. Each element has equal thickness (along y-direction) and height (along z-direction), and aspect ratio (width along -x-direction over height) is 0.25. The larger number of grids along x-direction used in the simulations is to better capture the heterogeneous plastic and elastic deformation along compression direction. The grid density along x- and y- directions used here has been examined to ensure the convergence of results.

An initial geometric perturbation was applied to the model in order to active the second mode of buckling corresponding to the periodic boundary condition, as illustrated in Fig. 3c. The initial sinusoidal waviness was applied to the model through applying the corresponding displacements to each element. The z-component of the displacement is a function of position x,

$$\mathbf{u} = (0,0,u_z),\ u_z = \delta \sin(2\pi x/\lambda) \tag{12}$$

where δ is the amplitude of the waviness, the wavelength λ equals to L_x for the second mode of buckling. The perturbation was introduced in the model through a pre-deformation gradient $\mathbf{F}_0$ with the component $F_{ij} = \delta_{ij} + u_{i,j}$ (δ_{ij} is the Kronecker delta function).

$$\mathbf{F_0} = \begin{bmatrix} 1 & 0 & 0 \\ 0 & 1 & 0 \\ \frac{2\pi\delta}{\lambda}\cos(\frac{2\pi x}{\lambda}) & 0 & 1 \end{bmatrix} \quad (13)$$

The $\mathbf{F_0}$ is considered as plastic deformation gradient $\mathbf{F_p}$ when initializing the parameters during the iteratively solving $\mathbf{F_p}$, $\mathbf{F_e}$, $\mathbf{L_p}$ and $\mathbf{S_p}$. To minimize the influence of the initial waviness on the buckling behavior, the amplitude to wavelength ratio δ/λ is set to be 0.001, which has been tested to ensure the convergence of the buckling strength and strain with respect to smaller amplitude to the wavelength ratio δ/λ. The $\mathbf{F_p}$ after perturbation in the three elements are the same along the thickness direction. In the simulation of buckling, compression strain is applied parallel to lamellae along the *x*-axis at a volume averaged deformation gradient rate, $\dot{\bar{F}}_{11} = -10^{-3}$/s, while the other two faces (along *y*- and *z*- directions) were free to expand. It is noted that the pre-deformation gradient F_0 shown in Eq. (13) is only one simple case associated with second mode buckling. The initial perturbations can be adjusted by varying the buckling mode and slenderness ratio according to experiments findings, or by introducing weak points in the model to simulate the local stress/strain concentration points associated with local defects in microstructure.

3.2 Slip systems in Al-Al$_2$Cu laminates

α-Al with face centered cubic structure has twelve {111}<110> slip systems. Due to the high stacking fault energy, Shockley partial dislocations are not considered in this study. The possible dislocation types in θ-Al_2Cu are directly related to its C16 body centered tetragonal structure. The most complete families of glide planes in θ are {110}, {100}, {011}, and {112}; The major slip systems include {110}<001>, $\{110\}\frac{1}{2}$<111>, {200}<001>, and $\{112\}\frac{1}{2}$<111> (Ignat and Durand, 1976). Using atomistic simulations, Zhou et al (Zhou et al., 2016a) recently studied the seven potential slip systems (110)<001>, (010)<001>, (310)<001>, (010)<100>, (110)<1 $\bar{1}$ 0>, $(110)\frac{1}{2}$<1$\bar{1}$1> and $(112)\frac{1}{2}$<$\bar{1}\bar{1}$1>, and found that these slips exhibit significantly higher Peierls barrier for glide at room temperature because the screw-type dislocations has a condensed core. Our recent experiments further demonstrated the less activity of these dislocations in nanoscale Al-Al$_2$Cu eutectics (Wang et al., 2018a). More importantly, our recent experiment study revealed that the nanoscale Al$_2$Cu lamellae, constrained by nanoscale Al, deform via defects not previously reported in monolithic Al$_2$Cu intermetallic: localized shear on $\{011\}_{Al2Cu}$ planes and

shear-induced faults on $\{121\}_{Al2Cu}$ planes (Wang et al., 2018a). Based on crystallographic analysis of slip continuity across the interface, the unexpected plasticity mechanisms are ascribed to the slip continuity across interface between α-Al and θ-Al_2Cu layers associated with the orientation relationship in Al-Al_2Cu eutectics. The results demonstrated that nanoscale microstructures promote plastic co-deformation in metallic composites with soft and hard phases. Corresponding to the characteristic orientation relationship $(001)_\alpha \| (001)_\theta$ and $[110]_\alpha \| [2\bar{1}0]_\theta$ (Wang et al., 2018a) in nano-scale Al-Al_2Cu eutectic alloy, we thus considered slips on four {121} planes for θ-Al_2Cu according to the slip continuity criterion. The four slip systems {121}<111> in Al_2Cu share the same slip traces with four of the twelve slips in Al on the interface plane. Moreover, the four {121} planes in Al_2Cu are nearly parallel to the four {111} planes in Al. Fig. 4 illustrates the slip systems in Al and Al_2Cu lamellae. There are totally four slip-pairs across the $(001)_\alpha \| (001)_\theta$ interface. They are $(2\bar{1}1)[\bar{1}\bar{1}1]$(#1) in Al_2Cu - $(111)[0\bar{1}1]$(#2) in Al, $(\bar{2}11)[111]$(#2) in Al_2Cu - $(\bar{1}\bar{1}1)[011]$(#3) in Al, $(121)[1\bar{1}1]$ (#3) in Al_2Cu - $(\bar{1}11)[101]$(#7) in Al, and $(\bar{1}\bar{2}1)[\bar{1}11]$(#4) in Al_2Cu - $(1\bar{1}1)[\bar{1}01]$(#9) in Al, as shown in Fig. 4a.

We first discuss the slip activity of different slip systems with respect to two unidirectional compressions, along $[001]_\alpha \| [001]_\theta$ which is normal to the interface, and $[110]_\alpha \| [2\bar{1}0]_\theta$ in the interface plane. The Schmid factor of these slips in Al and Al_2Cu are compared in Table 1. The red vectors in Al shown in Fig. 4 have non-zero Schmid factors, while the other <110> slip vectors in Al not shown in Fig. 4 are not activated due to zero Schmid factor. When the model is subjected to compression along $[001]_\alpha \| [001]_\theta$ (Fig. 4a), all the four paired slips in Al_2Cu are equally activated. When the model is subjected to compression along $[110]_\alpha \| [2\bar{1}0]_\theta$ (Fig. 4b), the activated slips are $(2\bar{1}1)[\bar{1}\bar{1}1]$(#1) in Al_2Cu - $(111)[0\bar{1}1]$(#2) in Al, and $(\bar{2}11)[111]$(#2) in Al_2Cu - $(\bar{1}\bar{1}1)[011]$(#3) in Al, while slips on the other two {121} planes of Al_2Cu are unlikely activated due to zero Schmid Factor.

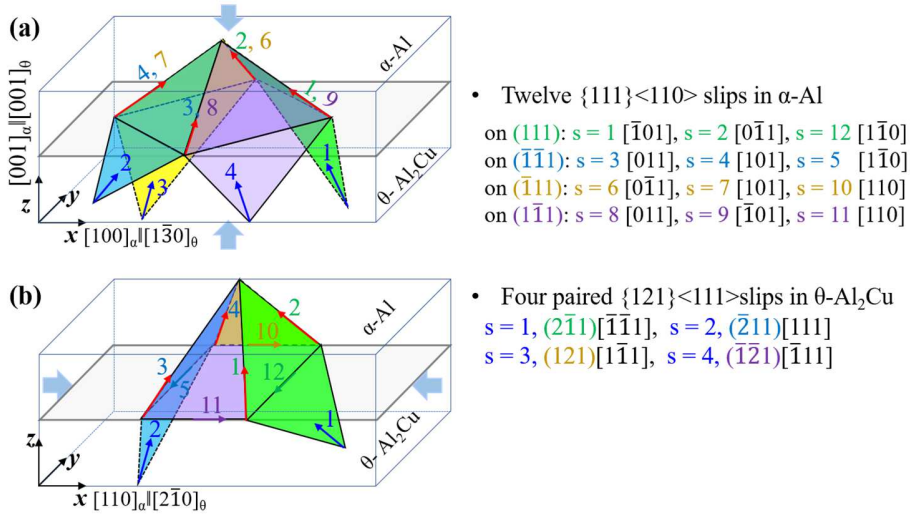

Fig. 4. Slip systems in upper α-Al and lower θ-Al_2Cu lamellae across the $(001)_\alpha \| (001)_\theta$ interface for compression strain is applied along (a) z-$[001]_\alpha \| [001]_\theta$ direction normal to interface and (b) $[110]_\alpha \| [2\bar{1}0]_\theta$ direction in the interface plane. The red and blue vectors on their corresponding slip planes are the activated slips in upper α-Al and lower θ-Al_2Cu respectively, and the vector numbers in Al are colored by their slip plane color.

Table 1. Schmid factor for the twelve {111}<110> slips in Al and four {121}<111> slips Al_2Cu corresponding to the four compression directions.

Compression axis	Schmid factor			
	$[001]_\alpha \| [001]_\theta$	$[110]_\alpha \| [2\bar{1}0]_\theta$	hard (+10°)	soft (−10°)
Al_2Cu	0.2402 (#1, #2)	**0.2402** (#1, #2)	**0.1098** (#1, #2)	**0.3563** (#1, #2)
Al_2Cu	0.2402 (#3, #4)	0.0 (#3, #4)	0.1305 (#3, #4)	0.1161 (#3, #4)
Al	0.4083 (#1-#4, #6-#9)	**0.4083** (#1-#4)	**0.3261** (#2, #3)	**0.4658** (#2, #3)
Al	0.0 (others)	0.0 (others)	0.4658 (#1, #4)	0.3261 (#1, #4)

3.3 Calibration of material parameters

Elastic constants for fcc-Al phase (Eisenlohr et al., 2013) and bct-Al_2Cu phase (Eshelman and Smith, 1978) are listed in Table 2a. The effective modulus predicted by spectral method for nanoscale Al-Al_2Cu eutectic alloy is in well agreement with the micropillar compression tests of an equal thickness Al-Al_2Cu composite with the layer thickness of 86 nm under compression normal to the lamellae, as shown in Fig. 5a. The parameters describing plastic deformation of Al and Al_2Cu layers, the thickness dependent g_0^s at a certain h, the reference slip rate $\dot{\gamma}_0$, and the rate sensitivity m in Eq. (5), were firstly determined by fitting the measured stress – strain curve of an Al-Al_2Cu micropillar which was compressed normal to the lamellae at a strain rate of 10^{-3}/s. In the simulation, compression strain is applied normal to lamellae at a volume averaged $\dot{\bar{F}}_{33} = -10^{-3}$/s. The fitted parameters for 86 nm Al-Al_2Cu micro-pillar were listed in Table 2a. Using

these parameters, the stress-strain curves and corresponding strain hardening rate predicted by our CLS-CP model are well consistent with experiment results, as shown in Fig. 5.

Table 2. Material parameters of Al and Al_2Cu used in the simulations.

(a) Constitutive parameters for the layer thickness of 86 nm under normal compression.

Parameters	Al	Al_2Cu
Elastic tensor C_{ij} (GPa)	C11 = 106.75 C12 = 60.41 C44 = 28.34	C11 = 179.66 C12 = 72.7 C33 = 170.23 C13 = 75.7 C44 = 27.98 C66 = 44.64
Reference slip rate $\dot{\gamma}_0$ (s^{-1})	0.0018	0.0006
Initial CRSS g_0^s (MPa)	56	680
Rate sensitivity m	0.0833	0.2

(b) Initial CRSS g_0^s for dislocation slips in Al and Al_2Cu, and the relative activity for dislocation slips in Al over in Al_2Cu layers used in the CLS-CP model to study buckling behavior under parallel compression.

	Layer thickness h (nm)				
	20	40	60	80	100
Al: g_0^s (MPa)	111	78	65	58	53
Al_2Cu: g_0^s (MPa)			680		
r_a	1.2	1.5	3	6	12

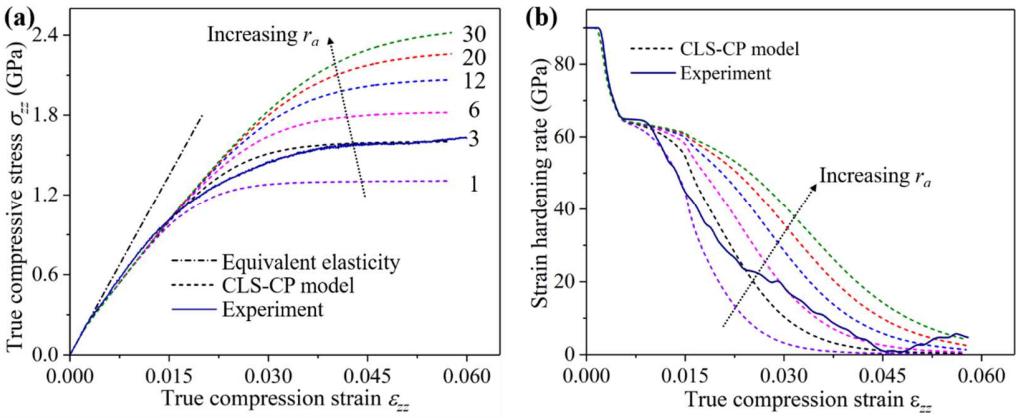

Fig. 5. (a) Compressive stress-strain curves and (b) corresponding strain hardening rate of Al-Al_2Cu nanolayers with layer thickness of 86 nm under compression normal to $(001)_\alpha \parallel (001)_\theta$ interface measured in micro-pillar compression experiment and predicted by the CLS-CP models with increasing relative dislocation activities in Al over that in Al_2Cu layer, $r_a = \dot{\gamma}_0^{Al}/\dot{\gamma}_0^{Al2Cu}$, varying from 1 to 30 representing increasing plastic incompatibility between the two layers.

The other essential parameters are calibrated as follows. Firstly, the initial yielding of Al-Al_2Cu multilayers starts with the motion of dislocations in Al layers. Thus, g_0^s for activating dislocation slip in Al layer is corresponding to the deviation of the experimentally measured curve from the linear response. It is determined to be 56 MPa for the 86 nm thick Al. Secondly, the slip rate sensitivity m for Al_2Cu is fitted to the experimental stress-strain curve after yielding, while a low m for Al equal to 0.0833 was chosen to simulate its nearly perfect plastic behavior

because no dislocation cells form in nanolayers. Thirdly, the thickness dependent CRSS for dislocations in Al layers were determined according to Eq. (9). Here, the thickness independent lattice friction τ_0 adopted the same value as that in bulk Al. The factor k in Eq. (9) was calculated as $k = \frac{(g_0^S - \tau_0)}{\mu} \frac{h}{b\ln(h/b)}$ using the fitted g_0^S at h = 86 nm. Last, to estimate the CRSS for dislocations in Al_2Cu layers, we conducted a series of simulations with varying the ratio of reference slip rate in Al over that in Al_2Cu phase, $r_a = \dot{\gamma}_0^{Al}/\dot{\gamma}_0^{Al2Cu}$, from 1 to 30. It is worth mentioning that the relative activity of dislocation slips in Al over that in Al_2Cu layers r_a does not change the yield stress (Fig. 5a) but significantly affects the strain hardening rate (Fig. 5b). From the viewpoint of the relative activity of different slip systems, the increase of r_a corresponds to the decrease of dislocation activity in Al_2Cu layer (this could be associated with the increase in the Al_2Cu layer thickness) and/or the increase of dislocation activity in Al layer (this could be associated with the increase in the Al layer thickness), the strain hardening rate of the composite will increase due to the plastic incompatibility between metal and brittle layers. Comparing the strain hardening rate at different r_a with experiment result in Fig. 5b, r_a = 3 is chosen in further simulations to obtain the CRSS for activating dislocation slip in Al_2Cu layers, which is determined to be 680 MPa by fitting the experimentally measured stress-strain curve. Table 2 lists all the material parameters used in the simulations. It is noted in Fig. 5b that r_a should vary with accumulated dislocation densities rather than a constant. For the first attempt, we adopted a constant r_a in the current model to simplify the description of the plastic incompatibility induced hardening based on the CLS mechanism. An appropriate r_a should be able to reproduce the strain hardening rate in experiments and well capture the difference of dislocation nucleation rate in the two layers. Further work to incorporate the dislocation activities in the metal and brittle layers as a function of the accumulated dislocations in the interface into CLS-CP model is in progress.

3.4 Comparison among one, three and five elements models

When plastic deformation is ensured to be constant through layer thickness, another important feature in our model is to capture the heterogeneous elastic deformation through layer thickness. As we pointed out before, the mesh with one element through one single layer may underestimate the heterogeneous elastic deformation through layer thickness. Here we compared the mesh effect on the stress-strain curves (Fig. 6a), distribution of equivalent plastic strain (Fig.

6b) and stress (Fig. 6c-f) in Al-Al_2Cu eutectic alloy. We simulate a 40 nm thick Al-Al_2Cu layered structure under a compression along $[110]_\alpha \| [2\bar{1}0]_\theta$ direction using CLS-CP model with one, three and five elements through the layer. The material parameters used are shown in Table 2b. For the five elements modeling, the plastic deformation in the middle element is firstly calculated based on the average stress among the five elements, then the plastic deformation gradient and plastic velocity gradient in the middle element are assigned to the other four elements, while the elastic deformation in each element is iteratively solved, which is similar to the flow chart illustrated for three elements case in Fig. 2b.

The stress strain curves in Fig. 6a indicate similar buckling instability when using three or five elements per layer. However, when each layer is meshed by only one element, the buckling instability does not occur even after the applied compression strain has reached 10%. As a matter of fact, no buckling instability was observed when the applied strain reached 20% in further compression. This is ascribed to the constant stresses through Al and Al_2Cu layers (Fig. 6d-f) associated with the single element through the layer. As a result, the net bending moment is zero.

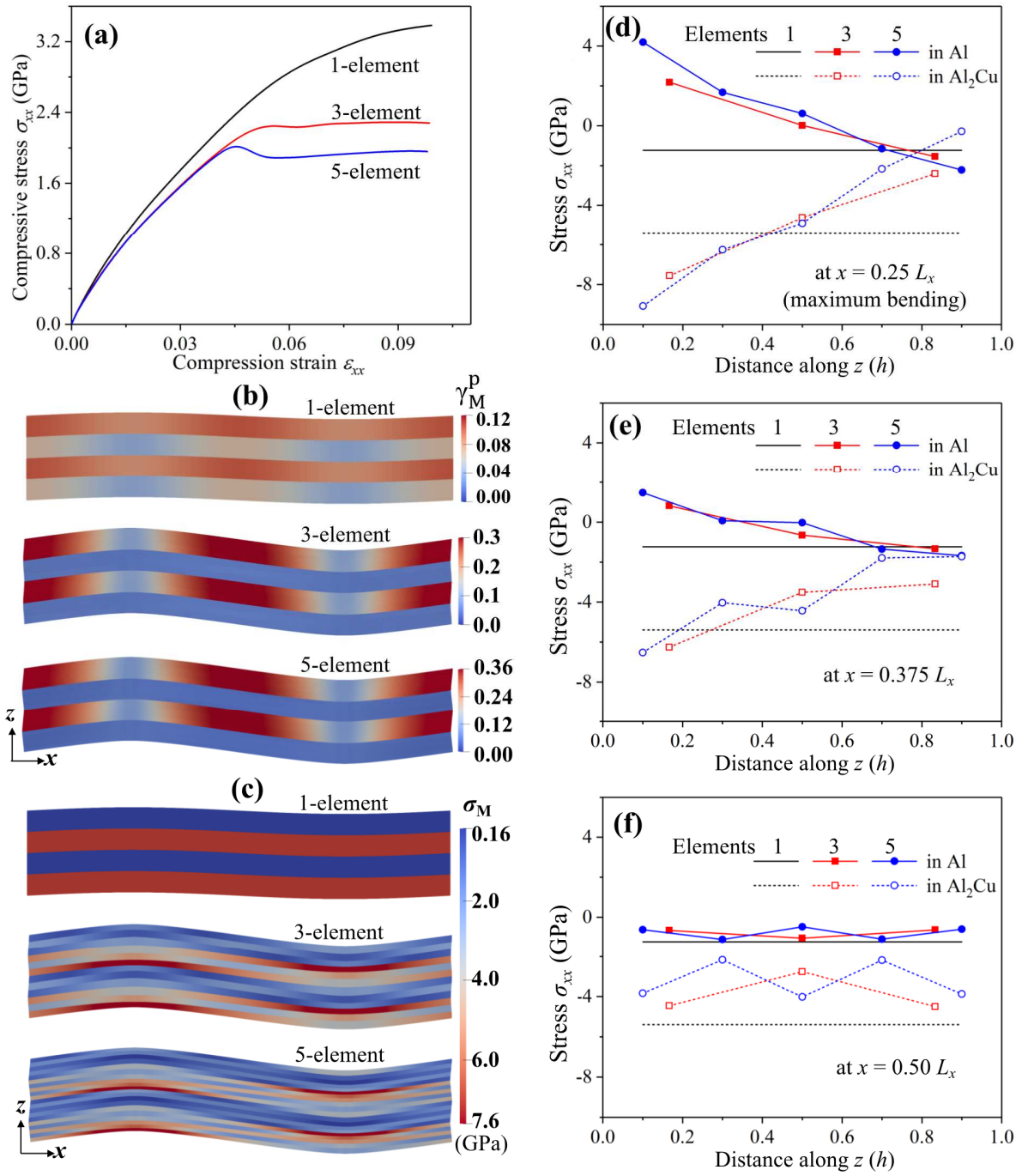

Fig. 6. Effects of heterogeneous elastic deformation through layer thickness on the deformation behavior of Al-Al_2Cu with layer thickness of 40 nm under compression along x-$[110]_\alpha \| [2\bar{1}0]_\theta$. (a) Stress-strain curves, (b-c) Distribution of Mises equivalent plastic strain γ_M^p and equivalent stress σ_M at a compression strain ε_{xx} = -7.78%. (d-f) Distribution of stress component σ_{xx} along z-direction in Al and Al_2Cu layers at x = 0.25 L_x, 0.375 L_x and 0.5 L_x at a compression strain ε_{xx} = -7.78%.

The heterogeneous elastic deformation through the layer thickness can be well captured by three or five elements. Fig. 6d-f shows the stress distribution when applied compression strain ε_{xx} is -7.78% at three representative positions, x = 0.25 L_x, 0.50 L_x and 0.375 L_x corresponding to maximum bending, maximum displacement gradient and middle position in between them respectively. Take the stress distribution along z-direction at maximum bending position (Fig. 6d) as an example, the three and five elements methods predict quite similar variation of the stress σ_{xx} in both Al and Al_2Cu layers along layer thickness, they both decrease (Al) or increase (Al_2Cu) with increasing distance from the interface and they both cross the stress predicted by one element method. This feature is consistent with the bending deformation occurred under uniform compression. Same conclusion can be reached for the stress at x = 0.375 L_x, as shown in Fig. 6e. For the stress at x = 0.5 L_x with maximum displacement gradient and maximum plastic deformation while less bending, both the three and five elements methods predict almost constant, smaller magnitude of stress in Al and Al_2Cu layers than those of one element prediction. Comparing these mechanical properties predicted by the CLS-CP model with three and five elements, we conclude that the CLS-CP model with three elements can effectively predict the heterogeneous elastic deformation through the thickness direction, and well capture the change of stress state in one layer from tension to compression stress at the maximum bending position. More elements for one layer may be needed to improve the accuracy of model predictions, especially for well capturing heterogeneous elastic deformation.

4. Modeling buckling response of Al-Al_2Cu eutectics

To demonstrate the predictive capability of our CLS-CP model, we simulate a 40 nm thick Al-Al_2Cu layered structure under a compression along $[110]_\alpha \| [2\bar{1}0]_\theta$ direction using CLS-CP model and standard CP models, and compared the predictions with experiment results. The constitutive parameters used in the CLS-CP model for the 40 nm thick Al and Al_2Cu are listed in Table 2. The reference slip rate in Al $\dot{\gamma}_0^{Al}$ is 10^{-3}/s for simplicity. Two reference slip rates in Al_2Cu, $\dot{\gamma}_0^{Al2Cu}$ = 10^{-3}/s and 10^{-4}/s corresponding to r_a = 1 and 10 respectively, were adopted in the simulations to examine the influence of dislocation activities in Al_2Cu on the mechanical properties of the alloy. These constitutive parameters for nanoscale Al lamellae are also used in standard CP model for comparison, referred to as CP-N. In addition, we also conducted standard CP simulations with bulk Al constitutive parameters, referred to as CP-B.

4.1. Stress-strain response and buckling feature

Fig. 7a shows stress-strain curves, revealing the occurrence of buckling instability when the applied compression strain reaches a critical value. One apparent observation is that both the CLS-CP and standard CP models predict the instability phenomenon when the applied compression strain exceeds a critical strain (referred to as buckling strain). The instability is indicated by (i) stress drop on the stress-strain curve (Fig. 7a), (ii) abrupt increase in the deflection (Fig. 7b), and (iii) jump of plastic strain in Al and Al_2Cu layers (Figs. 7c-7f). Once the instability happens, plastic deformation develops quickly, as indicated by the von Mises equivalent plastic strain in Al shown in Fig. 7c. The critical buckling strain and buckling strength predicted by the CLS-CP model are in reasonable agreement with those measured in micro-pillar test of the 40 nm thick Al-Al_2Cu lamellae under parallel compression, though they are slightly higher than the experiment results. The reason for this difference could be correlated to the simulation conditions. In experiments, different buckling modes can occur due to stress concentration associated with defects and microstructure, either the first or the second mode. In addition, the unavoidable defects could trigger the buckling instability. While in simulations, we adopted the second mode buckling corresponding to the periodic boundary condition along the compression direction. Compared to CLS-CP model, CP-B model predicts a much smaller buckling strain around 1.3%, compared with 3.5% in experiments and 4.4% in CLS-CP model. Even if adopting nanolayer Al properties, the CP-N model still underestimates the buckling strain 3.0%. These results predicted by CP-B and CP-N are ascribed to the lack of the constraint of the CLS deformation mechanism.

In addition to the difference in the critical buckling strain, CLS-CP and CP models predict either softening or hardening phenomena after the occurrence of the buckling instability. To reveal the correlation of deformation behaviors with plastic deformation in Al and Al_2Cu layers, we first discuss the dominant slip systems according to the crystallography analysis, and further compute plastic strains in the layer with respect to slip systems, as shown in Figs. 7c-7f. Slips associated with slip systems #1-#4 in Al will rotate the layer, accommodating the bending of Al_2Cu lamellae. Once crystal rotation commences, dislocation slips associated with slip systems $(\bar{1}11)[110]$ and $(1\bar{1}1)[110]$ (#10 and #11 in Fig. 4b) will be activated. Other slip systems are seldomly activated because of zero Schmid factor. As demonstrated in Fig. 7d, dislocation slips

associated with slip systems #1-#4 are activated during compression, but dislocation slips associated with slip systems #10 and #11 are activated after the instability happens.

In the case of CLS-CP model, strain hardening occurs if there is strong incompatibility of plastic deformation between Al layer and Al_2Cu layer (corresponding to r_a = 10, a low slip activity in Al_2Cu), or strain softening takes place if plastic deformation is easily activated in Al_2Cu layer (corresponding to r_a = 1, a high slip activity in Al_2Cu). The results in Fig. 7a revealed that the critical buckling strain and corresponding stress are independent on the ratio of reference slip rates r_a. However, the continuous mechanical response is strongly correlated to the ratio r_a, implying that strain hardening is dominated by plastic incompatibility between soft and hard layers. For a low slip activity in Al_2Cu (r_a = 10), relatively high strain hardening is observed until the applied strain increases to a critical strain about 6%, where plastic instability occurs in Al_2Cu, corresponding to the sharp increase in plastic strain on systems #1-#4 in Al_2Cu layer as shown in Fig. 7e. It is noted that dislocation slips in Al_2Cu associated with slip systems #1 and #2 were activated earlier than buckling instability but slip systems #3 and #4 were activated after buckling occurs. This is due to nonzero Schmid factor for slip systems #1 and #2 and zero Schmid factor for slip systems #3 and #4 before buckling. Once buckling takes place, lattice rotation results in non-zero Schmid factor for slip systems #3 and #4.

In the cases of CP models, the CP-N model with r_a = 10 predicts over-softening phenomenon after buckling instability occurs, as shown in Fig. 7a. However, the CP-B model with r_a = 10 predicts noticeably strain hardening due to lateral hardening, and a second instability after the compressive strain reaches about 2.5%, as shown in Fig. 7a. The occurrence of the second instability is related to the activation of #10 and #11 slips in the elements connected to interfaces, as shown by the jump of plastic strain on slip systems #10 and #11 in the lower and upper elements of Al, $\gamma^{(s)}(i = 1)$ and $\gamma^{(s)}(i = 3)$ in Fig. 7f. More details of plastic deformation in Al and Al_2Cu layers will be discussed in the following section.

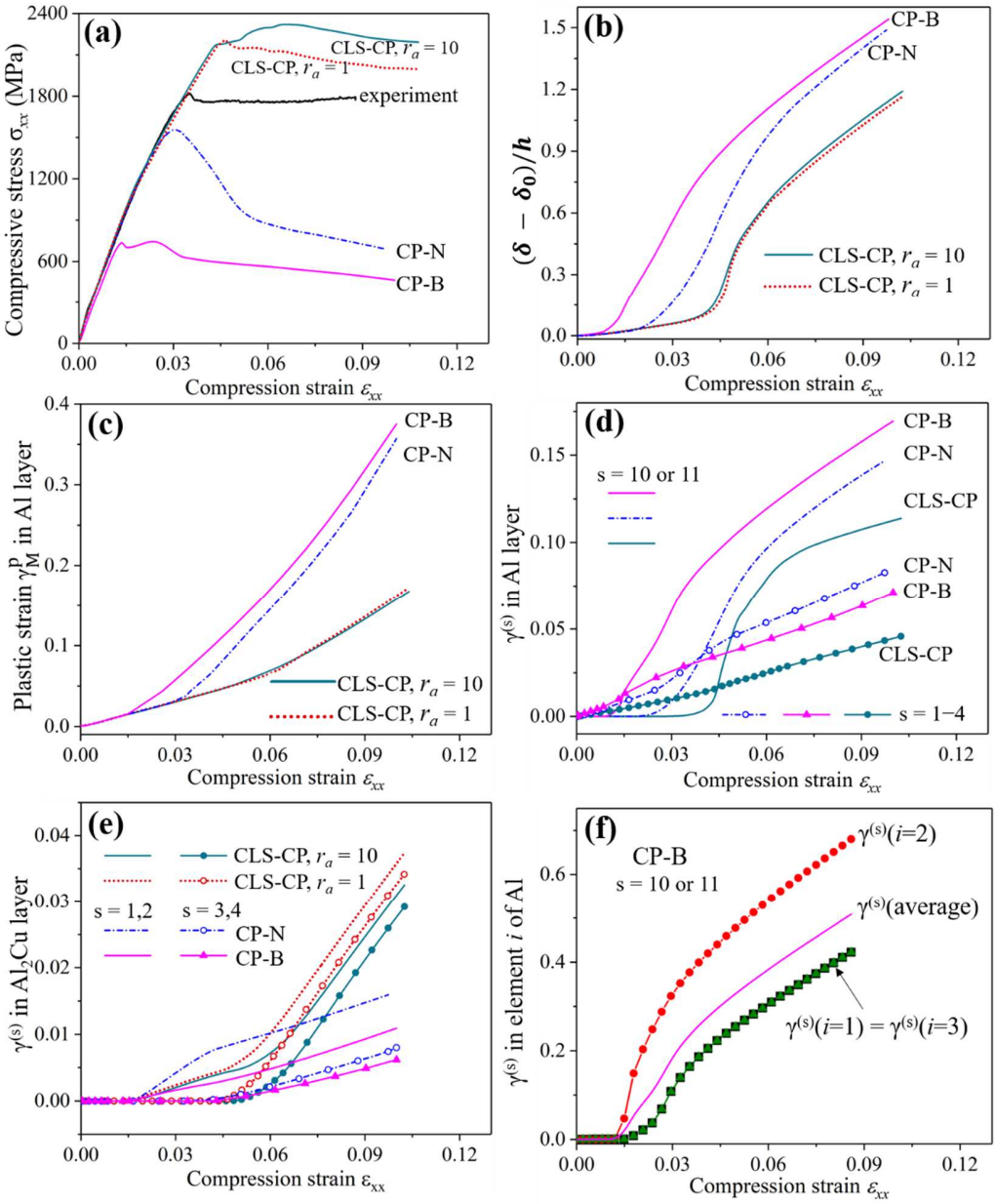

Fig. 7. Mechanical response of Al-Al_2Cu composites with lamellar spacing of 40 nm under compression strain applied along x-$[110]_\alpha \parallel [2\bar{1}0]_\theta$ direction predicted by the CLS-CP (r_a = 10, 1) and standard CP models adopting either nanolayer Al (CP-N) or bulk Al (CP-B) constitutive parameters. (a) Average true stress-true strain curves, (b) deflection δ normalized by the thickness h and (c) Mises equivalent plastic strain in Al layer averaged over all elements of Al layers. (d-e) Evolution of accumulated plastic strain on s-th slip system averaged in all elements of (d) Al and (e) Al_2Cu layers respectively. The magnitude of $\gamma^{(s)}$ in Al layer predicted by CP-N and CP-B models shown in (d) is one third of the actual magnitude. (f) The accumulated plastic strain on s-th slip system in the lower (i = 1), middle (i = 1) and upper (i = 3) elements in Al and their average.

4.2. Plastic deformation distribution along and through layers

Figs. 8a-c display the distribution of von Mises equivalent plastic strain $\gamma_{\mathrm{M}}^{\mathrm{p}}$ along and through the layers predicted by the CLS-CP and CP models, respectively. The CLS-CP model predicts identical plastic strain through the layer thickness (Fig. 8a), while the CP model predicts heterogeneous plastic strain through the layer thickness (Figs. 8b and 8c). More importantly, the CLS-CP model predicts smaller plastic strain in Al layers than that in CP models. For example, the peak strain is 0.34 for the CLS-CP model but 0.66 for CP models (Fig. 8d). In addition, the CP models predict that plastic strain is localized in the middle element in Al lamellae, and small plastic strain happens in the elements connected to interfaces. On the other hand, all models predict inhomogeneous plastic strain along the layers after bending occurs. However, the inhomogeneity shows distinct feature in Al and Al_2Cu layers, as shown in Figs. 8d-8i.

As for plastic strain in Al layers, regardless of models and material parameters, Al layers experience smaller plastic strain in the maximum bend regions than that in the rest of the layer, as shown in Figs. 8d-8f. However, in the case of CP models, the plastic strains in the three elements have different distributions along the Al layer. As shown in Figs. 8e and 8f, the plastic strain in the middle elements $\gamma_{\mathrm{M}}^{\mathrm{p}}(i = 2)$ exhibits a similar feature to the averaged plastic strain (solid line) of the three elements. The peaks of plastic strains in the lower $\gamma_{\mathrm{M}}^{\mathrm{p}}(i = 1)$ and upper $\gamma_{\mathrm{M}}^{\mathrm{p}}(i = 3)$ elements shift towards the right or left relative to the peak of the averaged plastic strain, while the valleys of plastic strains in the lower $\gamma_{\mathrm{M}}^{\mathrm{p}}(i = 1)$ and upper $\gamma_{\mathrm{M}}^{\mathrm{p}}(i = 3)$ elements remain in the maximum bend regions. The constitutive parameters used in CP models don't change these features, but slightly affect the magnitude of plastic strains.

Regarding plastic strain in Al_2Cu layers (Figs. 8g, 8h and 8i), the CLS-CP model predicts larger plastic strain in the maximum bend regions (Fig. 8g), but CP models predict smaller plastic strain in the maximum bend regions (Fig. 8g). More importantly, the CLS-CP model predicts greater plastic strain than CP models, indicating that our CLS-CP model to some extent ensures plastic co-deformation corresponding to the CLS mechanism in nanoscale laminates.

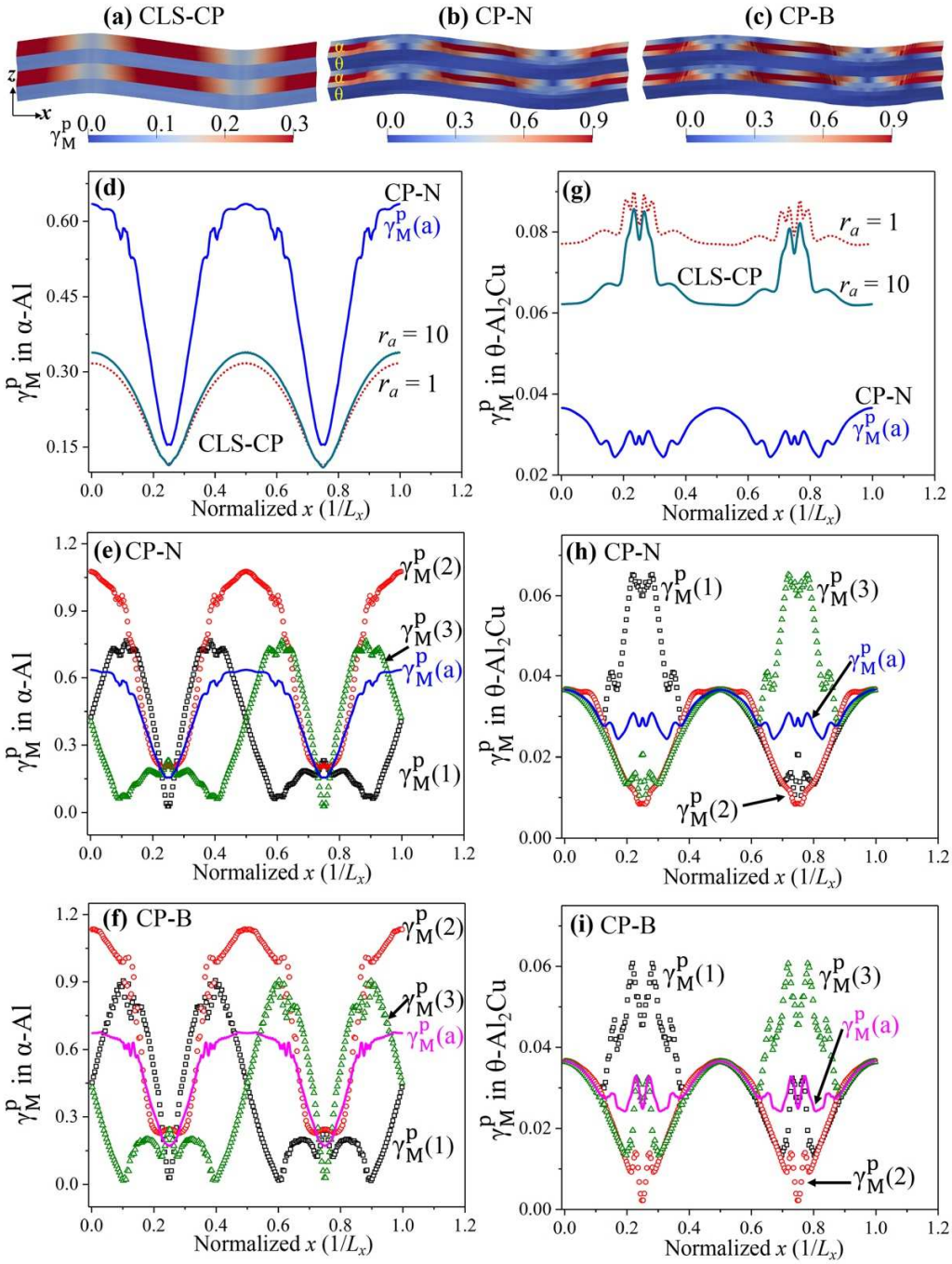

Fig. 8. (a-c) Distribution of von Mises equivalent plastic strain γ_M^p in Al-Al_2Cu alloy at compression strain ε_{xx} = -7.78% predicted by CLS-CP, CP-N and CP-B models. (d-i) Distribution of γ_M^p along x direction. $\gamma_M^p(i)$ with i = 1, 2, 3, refers to the γ_M^p in the lower, middle or upper element of Al (d-f) and Al_2Cu (g-i) layer. $\gamma_M^p(a)$ refers to the averaged Mises equivalent plastic strain of the three elements through the layer thickness.

4.3. Stress distribution along and through layers

Figs. 9a-c display the distribution of von Mises stress σ_M along and through the layers at a compression strain ε_{xx} = -7.78%. All the models predict inhomogeneous stress along the layers and through the layer thickness. For example, in Al_2Cu layers all the models predict a peak stress σ_M in the maximum bend regions (lower element at $x = 0.25\ L_x$ and upper element at $x = 0.75\ L_x$) which is associated with the maximum compressive stress σ_{xx} in those regions. Corresponding to uniaxial compression along the x-axis, the following analysis is focused on the distribution of stress σ_{xx} along and through the layers, as shown in Figs. 9d-g. Since the distribution of Mises plastic strain and Mises stress predicted by CP-N and CP-B models show similar feature, the following comparison of distribution of stress σ_{xx} will use CP-N model predictions representing CP model for brevity.

As for the stress in Al_2Cu layer, Figs. 9d and 9e compared the stresses σ_{xx}^i and σ_{xx}^a that are predicted by the CLS-CP and CP models. The superscript i in σ_{xx}^i indicates the element number through the layer thickness. The lower, middle and upper elements in each layer are denoted as i = 1, 2, 3 respectively. σ_{xx}^a represents the average stress among the three elements. Take the maximum bend region at $x = 0.25\ L_x$, the CLS-CP model predicts compressive stress in the three elements as shown in Fig. 9d. This explains the experimental observation that the bend region doesn't crack in Al_2Cu layer in nanoscale Al-Al_2Cu eutectic alloy (Wang et al., 2018b). However, at $x = 0.25\ L_x$, the CP model predicts tensile stress σ_{xx}^3 in the upper element as shown in Fig. 9e. The maximum tensile stress in Al_2Cu could induce mode-I crack, as observed in as-cast Al-Al_2Cu alloy (Wang et al., 2018b). This comparison implies that the CLS-CP model can predict the stress distribution in the nanoscale metal-intermetallic layers in bending deformation, while the standard CP model is more suitable for microscale layered structures.

As for the stress in Al layers, CLS-CP and CP model predict a similar distribution of the average stress σ_{xx}^a along the layers, as shown in Figs. 9f and 9g. The maximum bend regions (x = 0.25 L_x and 0.75 L_x) is subjected to the maximum average tensile stress σ_{xx}^a, and the least bend regions (0, 0.5 L_x and 1.0 L_x) is subjected to the maximum compressive stress σ_{xx}^a. However, the stresses σ_{xx}^i in the three elements through the layer thickness have different magnitudes and signs. Take the maximum bend region at $x = 0.25\ L_x$ as an example, the CLS-CP model predicts a tensile stress σ_{xx}^1 (= 2.8 GPa) in the lower element and a compressive stress σ_{xx}^3 (= -2 GPa) in

the upper element. But the CP model predicts a smaller tensile stress $\sigma_{xx}^{1}$and σ_{xx}^{3} (= 0.5 GPa) in both lower and upper elements, as shown in Figs. 9f and 9g. The larger tensile stress in Al predicted by the CLS-CP model implies that a local disorder structure could occur in the bend region of Al layers in nanoscale Al-Al_2Cu eutectic alloy under compression parallel to lamellae. Such phenomena have been observed in Al-TiN multilayers (Li et al., 2014; Li and Wang, 2015).

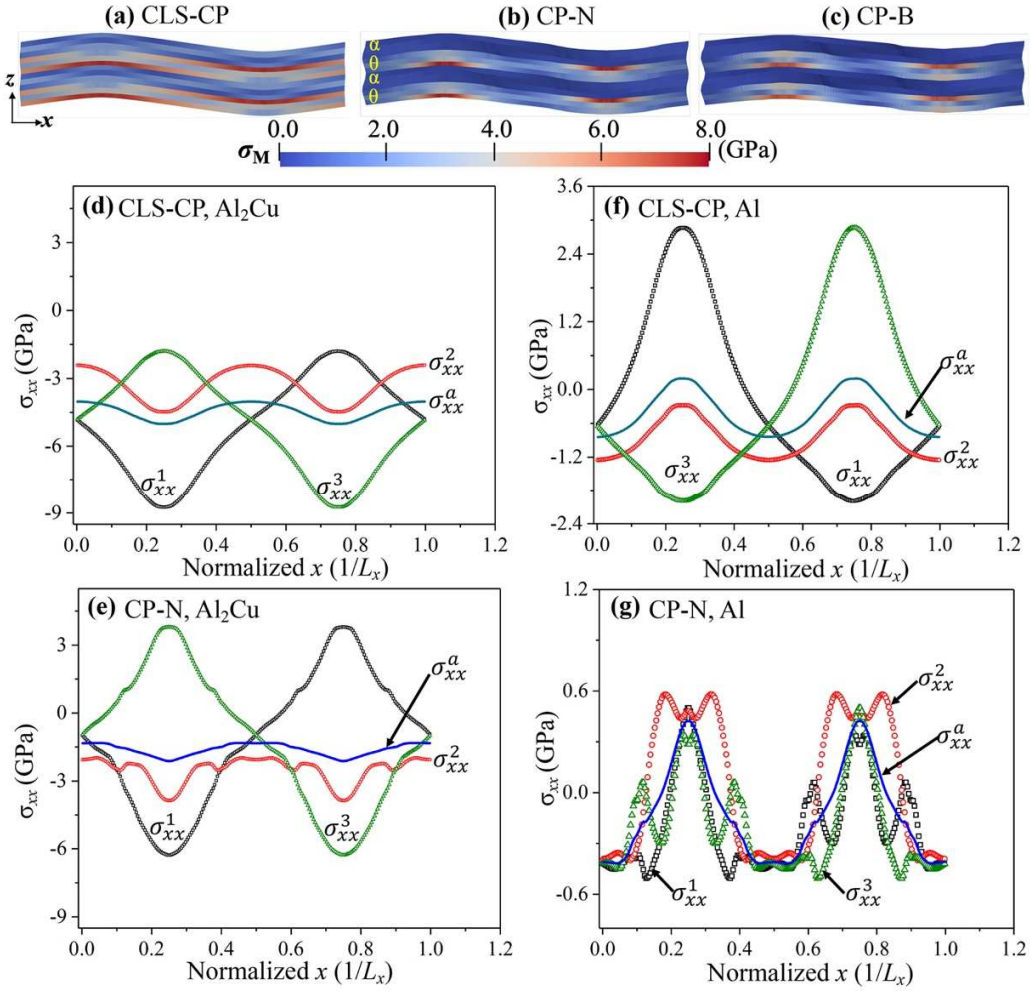

Fig. 9. Distribution of (a-c) von Mises equivalent stress σ_M in Al-Al_2Cu alloy at compression strain ε_{xx} = -7.78% predicted by CLS-CP and CP-N models. (d-g) Distribution of Cauchy stress component σ_{xx} along x direction. $\sigma_{xx}^{i}$with i = 1, 2, 3, refers to σ_{xx} in the lower, middle and upper element of Al or Al_2Cu layer respectively, and σ_{xx}^{a} refers to the averaged σ_{xx} of the three elements through one layer.

The large tensile stress in Al layer after bending predicted by the CLS-CP model shown in Fig. 9f is attributed to the CLS deformation mechanism which enforces the same plastic strain through the layer thickness. As applied compressive strain ε_{xx} increases, CLS-CP model predicts

same plastic strain in the three elements, γ^{p}_{xx}, at the maximum bend region of Al layers (for example at x = 0.25 L_x), and it continuously increases, as shown in Fig. 10a. Before bending, all the three elements are under compression stress, as indicated by the negative stress σ^{i}_{xx} (below the dashed line) in Fig. 10b. After bending occurs, the average stress at x = 0.25 L_x is positive in Al (σ^{a}_{xx} in Fig. 10b) but negative in Al_2Cu (σ^{a}_{xx} in Fig. 9e), thus bending induced strain in Al layer is positive. Considering the geometry continuity between the boundary elements of Al and Al_2Cu layers, we can infer the upper Al element, connecting to the lower Al_2Cu element which is under maximum compression, is in transition region from tension to compression. Therefore, the lower Al element, connecting to the upper Al_2Cu element which is already under bending induced tensile strain, should be under tensile strain due to bending deformation. In the meanwhile, plastic strain in the lower element of Al layer is compressive. To accommodate the bending induced tension in Al layer, a large tensile elastic strain occurs in the lower element (i = 1) of Al layer. As a result, a large tensile stress σ^{1}_{xx} develops in the lower element of Al layer, as shown in Fig. 10b.

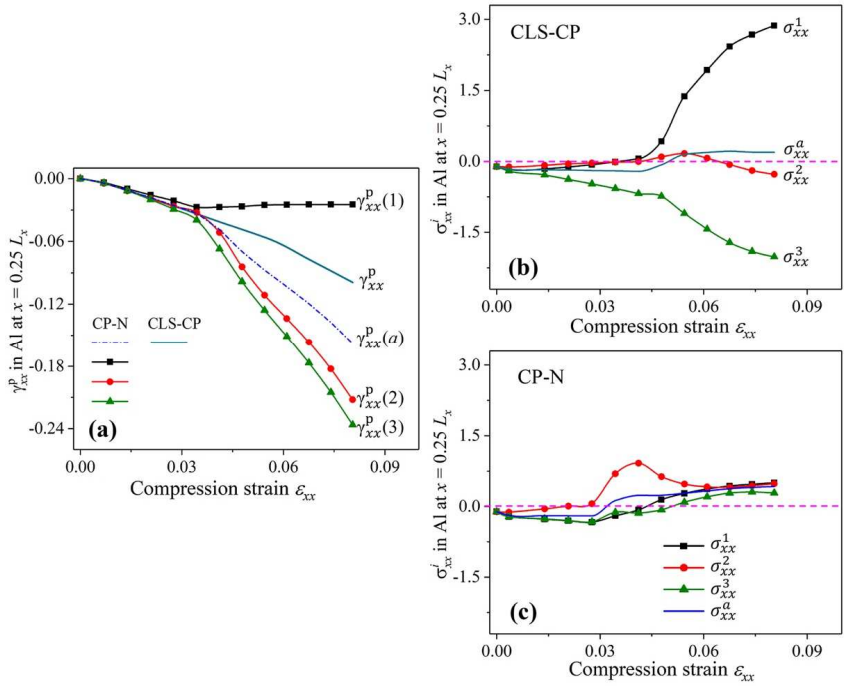

Fig. 10. Variation of (a) plastic strain component $\gamma^{\mathrm{p}}_{xx}(i)$ and (b-c) Cauchy stress component σ^{i}_{xx} in the three elements (i = 1, 2, 3) of Al layer and their averages (i = a) among the three elements at maximum bend position x = 0.25 L_x with increasing applied compressive strain ε_{xx}. γ^{p}_{xx} is the same plastic strain in the three elements of Al layer predicted by the CLS-CP model.

However, the tensile stress in Al layer is of much lower magnitude in the case of CP model. It is because the plastic deformation in the three elements individually evolves to relax the stress in Al layer. For example, due to no interface constraint on the middle element, it undergoes much larger plastic deformation than the average plastic deformation, as indicated by larger magnitude of $\gamma_{xx}^{\mathrm{p}}(i = 2)$ than $\gamma_{xx}^{\mathrm{p}}(a)$ in Fig. 10a. For the lower and upper elements, to accommodate the bending induced tensile and compressive strain, the compressive plastic strain, $\gamma_{xx}^{\mathrm{p}}(i = 1)$ and $\gamma_{xx}^{\mathrm{p}}(i = 3)$ are much smaller or larger than the $\gamma_{xx}^{\mathrm{p}}(a)$ respectively. As a result, the stress in the three elements are low, as shown in Fig. 10c.

4.4. Effect of layer thickness on deformation behavior

Using the CLS-CP model, we studied the effect of the layer thickness on the buckling behavior of Al-Al_2Cu eutectic alloy. In our simulations, the thickness effect is taken into account through tuning CRSS for dislocation slip $g_0^s(b^s, h)$, which obeys the Orowan type relation described in Eq. (9), and the relative activity r_a of slips in the Al and Al_2Cu layers, which describes the plastic co-deformation ability of the composites (Wang and Misra, 2014). The parameters adopted in our simulations are listed in Table 2b. The relative activity r_a gradually increases with the increasing thickness h, which reflects the tendency of the slip activity decrease in Al_2Cu layer with the increase in the Al_2Cu layer thickness and/or the dislocation activity increase in Al layer with the increase in the Al layer thickness. Fig. 11 shows the stress-strain curves predicted by the CLS-CP model. The simulation results indicate that the buckling strength and the critical strain decreases with increasing layer thickness.

The higher buckling strength and strain at smaller layer thickness can be understood from the co-deformation between adjacent layers. Under a compression along $[110]_{Al}$ direction, net plastic deformation on systems #1-#4 in Al layers shown Fig. 4b will cause Al lamellae to rotate and shrink. Al_2Cu lamellae will bend to accommodate this rotational deformation in Al lamellae. When CRSS for dislocation slip in Al increases with decreasing thickness h, the resistance to rotation of Al layer associated with dislocation gliding through the layers increases with the decrease in layer thickness h, resulting in stronger resistance to Al_2Cu bending. Therefore, buckling strength and strain increase as thickness decreases.

The curves shown in Fig. 11 also demonstrated the strain hardening after instability due to strong plastic incompatibility between the two layers, considering we used a larger r_a at larger

layer thickness. When we used smaller r_a to reflect more active dislocation activity in Al_2Cu layer in the case of smaller layer thickness, the softening will occur as a result of plastic instability in Al_2Cu layers, similar to the results discussed in section 4.1.

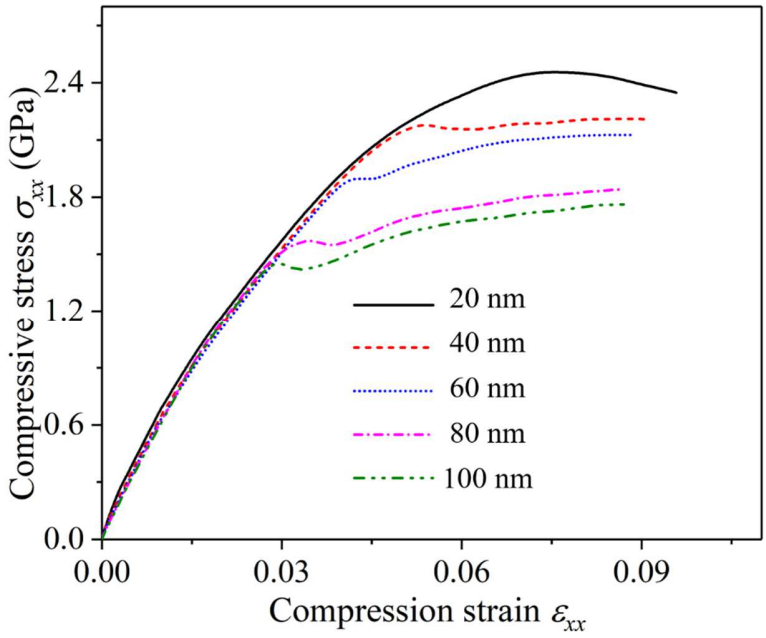

Fig. 11. Effects of the layer thickness on stress-strain curves under parallel compression along $[110]_\alpha \| [2\bar{1}0]_\theta$ direction predicted by the CLS-CP model.

4.5. Effect of loading direction on deformation behavior

To reveal the effect of crystallographic anisotropy on mechanical response, we compared the stress-strain curves in Fig. 12a and the evolution of plastic strain in Al_2Cu (Fig. 12b) and Al (Fig. 12c) layers of Al-Al_2Cu nanolaminates in response of four uniaxial compression loadings, normal to lamellae, and parallel to lamellae along three directions $[110]_\alpha \| [2\bar{1}0]_\theta$ (referred to as $[110]_\alpha$), and +10° and −10° clockwise deviating from the $[110]_\alpha$, referred to as hard and soft directions respectively. The hard or soft direction corresponds to the Schmid Factor (Table 1) for the paired slips in Al and Al_2Cu are smaller or larger compared with those for the compression along $[110]_\alpha$. The Schmid factors associated with twelve {111}<110> dislocation slips in Al and four paired {121}<111> slips in Al_2Cu (see Fig. 4) are listed in Table 1. For the latter three in-plane compression directions, we focus on the plastic deformation on slip systems #1-4 in Al because they are activated to rotate the layers requiring Al_2Cu layer to buckle or plastic deform to accommodate this rotation. And particular attention was paid to plastic deformation on slip

system #2 in Al which is coupled with #1 in Al_2Cu, and #3 in Al coupled with #2 in Al_2Cu due to slip continuity. Material parameters for layer thickness of 40 nm listed in Table 2b were used in the simulations.

The stress-strain curves under the three in-plane compression directions show that, as the compression direction changes from a relatively hard direction for plastic deformation in both Al and Al_2Cu layers to a relatively soft direction, similar buckling instability occurs, but critical strain associated with instability increases, while critical strength slightly decreases. This is attributed to the successively activated plastic deformation in Al_2Cu layer, as shown by the plastic strain on the paired slip systems in Al_2Cu layer in Fig. 12b. For the soft compression direction, plastic deformation in Al_2Cu was activated earlier at a smaller applied strain due to its larger Schmid factor. Therefore, Al_2Cu layer is more likely to plastic co-deform with Al layer, which can accommodate part of the lattice rotation caused by plastic deformation in Al layer, thus postponing the occurrence of buckling instability. The evolution of plastic strain on these slip systems in Al_2Cu (Fig. 12b) and Al (Fig. 12c) layers further confirms the more/less active dislocation slips under soft/hard compression directions before buckling instability.

In the case of compression direction normal to the lamellae, the flow stress is lower than that under $[110]_\alpha$ compression, as shown in Fig. 12a. It is consistent with the activated dislocation slips in Al and Al_2Cu layers, as indicated by the plastic strain on those slip systems shown in Fig. 12b and 12c. Under normal compression, slip systems #1-4, #6-9 in Al are symmetrically activated, and the four paired {121}<111> slips in Al_2Cu are also symmetrically activated. Activation of these symmetrical slip systems in Al layers do not cause layer rotation. Their Schmid factors are equal to the corresponding ones for compression along $[110]_\alpha$ direction. However, the number of activated slip systems in both Al and Al_2Cu layers under $[110]_\alpha$ compression are only half of those activated under normal compression, and the asymmetrically activated dislocation slips in Al layer will result in layer rotation and further buckling of Al_2Cu layer. The more activated dislocation slips in Al_2Cu layer together with the symmetrical dislocation slips in Al layers, as can be seen from Fig. 12b and 12c, explains the relatively lower strength for the normal compression. These results demonstrated that the CLS-CP model can effectively predict the plastic anisotropy in nanolayered composites.

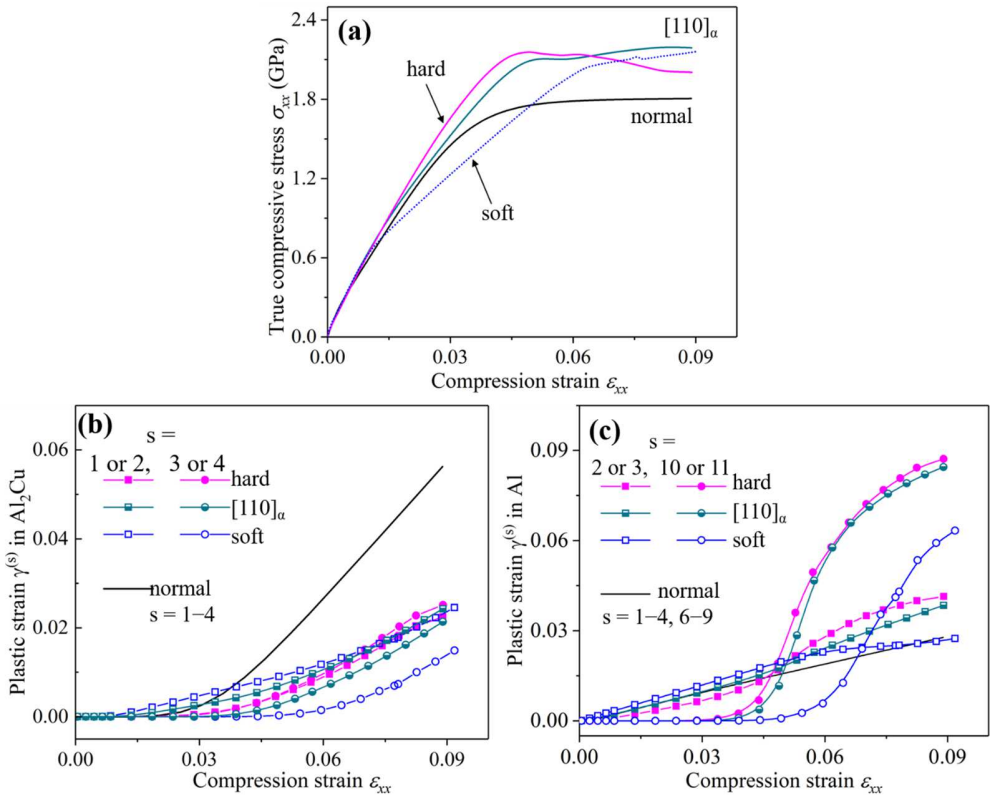

Fig. 12. Effects of loading direction on the deformation behavior. (a) Stress-strain curves and (b-c) evolution of plastic strain on *s*-th slip systems in Al_2Cu (b) and Al (c) layers in response of compression normal to the $(001)_\alpha \| (001)_\theta$ interface and along three directions in $(001)_\alpha$ plane, which are $[110]_\alpha \| [2\bar{1}0]_\theta$, +10° (hard) and −10° (soft) clockwise deviating from $[110]_\alpha$ direction respectively.

5. Conclusions

A mesoscale crystal plasticity model based on the CLS mechanism (CLS-CP) is developed to study the buckling behavior of nanolaminates that are composed of alternate soft metal and hard intermetallic layers. Corresponding to the CLS mechanism, constant plastic deformation and heterogeneous elastic deformation through the layer thickness are captured in the CLS-CP model through meshing each lamella with three or more elements and enforcing the same plastic deformation in these elements through the thickness. The plastic deformation in α-Al with face centered cubic structure is accounted for by dislocation gliding on twelve {111}<110> slip systems. Based on recent experiments, the plastic deformation of θ-Al_2Cu with C16 body centered tetragonal structure in nanoscale Al-Al_2Cu eutectic alloy is carried out through paired slips associated with {121}<111> slip systems. The present model can be further modified to

consider interface shear and slips parallel to interfaces in nanolaminates by differentiating the slips along interface and other slips.

Model parameters are calibrated by fitting experimental measured stress-strain curves of Al-Al_2Cu eutectic alloy under uniaxial compression normal to interfaces. The CLS-CP model predicts buckling instability of Al-Al_2Cu eutectic alloy when uniaxial compression is parallel to interfaces. In contrast, we also studied buckling instability of Al-Al_2Cu eutectic alloy using the standard crystal plasticity model where the plastic deformation through the thickness of a single lamella is individually calculated. Though both models can predict buckling instability of laminates, only the CLS-CP model is capable of predicting the mechanical response of co-deformation of Al-Al_2Cu nanolaminates and key features of confined layer slip, while the standard CP model is more suitable for studying the mechanical response of laminates with micrometers thick layers.

The CLS-CP model is demonstrated to be effective in predicting the thickness effects on the mechanical properties. Simulation results show that as layer thickness decreases, buckling instability occurs at a higher stress and a higher applied strain. It is the collective results of higher CRSS for dislocation slip in Al layers based on CLS mechanism and increasing dislocation activity in Al_2Cu layers. For example, 20 nm thick Al-Al_2Cu eutectics exhibit twice buckling strength than 100 nm layers. In addition, the model is capable of predicting the anisotropic effects of plastic deformation of Al and Al_2Cu crystals on the mechanical properties, i.e. buckling instability occurring at a smaller buckling strain is predicted for the compression along a relatively harder loading direction to active plastic slip in Al_2Cu layers, which is like the early instability occurred in submicron scale Al-Al_2Cu eutectics, where Al_2Cu layer is brittle. Last, the failure mechanism of the eutectics implied in the stress distribution and plastic co-deformation mechanism of the two layers well explained the seldomly observed tensile stress induced mode-I crack in the maximum bending regions of Al_2Cu, but multiple shears across Al_2Cu layer due to slip continuity and ductile fracture of Al layer reported in our previous experiments (Wang et al., 2018b).

Acknowledgement

This research is sponsored by DOE, Office of Science, Office of Basic Energy Sciences with the grant number of DE-SC0016808. Crystal plasticity simulations were completed utilizing the

Holland Computing Center of the University of Nebraska, which receives support from the Nebraska Research Initiative. Helpful discussion with Dr. Yao Shen, and useful suggestions from Dr. Martin Diehl in our early attempt to implement our model into DAMASK, were greatly appreciated.

Reference

Albiez, J., Erdle, H., Weygand, D., Böhlke, T., 2019. A gradient plasticity creep model accounting for slip transfer/activation at interfaces evaluated for the intermetallic NiAl-9Mo. Int. J. Plast. 113, 291-311.

Anderson, P., Foecke, T., Hazzledine, P., 1999. Dislocation-based deformation mechanisms in metallic nanolaminates. MRS Bulletin 24, 27-33.

Anderson, P.M., Li, C., 1995. Hall-Petch relations for multilayered materials. Nanostructured Mater. 5, 349-362.

Ardeljan, M., Knezevic, M., Jain, M., Pathak, S., Kumar, A., Li, N., Mara, N.A., Baldwin, J.K., Beyerlein, I.J., 2018. Room temperature deformation mechanisms of Mg/Nb nanolayered composites. J. Mater. Res. 33, 1311-1332.

Asaro, R.J., 1983. Micromechanics of Crystals and Polycrystals, in: Hutchinson, J.W., Wu, T.Y. (Eds.), Adv. Appl. Mech. Elsevier, pp. 1-115.

Bassani, J.L., Wu, T.-Y., 1991. Latent hardening in single crystals. II. Analytical characterization and predictions. Proc. R. Soc. Lond. A 435, 21-41.

Beyerlein, I.J., Wang, J., Zhang, R., 2013. Mapping dislocation nucleation behavior from bimetal interfaces. Acta Mater. 61, 7488-7499.

Bhattacharyya, D., Mara, N.A., Dickerson, P., Hoagland, R.G., Misra, A., 2010. A transmission electron microscopy study of the deformation behavior underneath nanoindents in nanoscale Al–TiN multilayered composites. Philos. Mag. 90, 1711-1724.

Burbery, N.B., Po, G., Das, R., Ghoniem, N., Ferguson, W.G., 2017. Dislocation dynamics in polycrystals with atomistic-informed mechanisms of dislocation - grain boundary interactions. J. Micromech. Mol. Phys. 02, 1750003.

Chawla, N., Singh, D., Shen, Y.-L., Tang, G., Chawla, K., 2008. Indentation mechanics and fracture behavior of metal/ceramic nanolaminate composites. J. Mater. Sci. 43, 4383-4390.

Cho, J., Molinari, J.-F., Curtin, W.A., Anciaux, G., 2018. The coupled atomistic/discrete-dislocation method in 3d. Part III: Dynamics of hybrid dislocations. J. Mech. Phys. Solids 118, 1-14.

Choudhuri, D., Banerjee, R., Srinivasan, S., 2018. Uniaxial deformation of face-centered-cubic (Ni)-ordered B2 (NiAl) bicrystals: atomistic mechanisms near a Kurdjumov–Sachs interface. J. Mater. Sci. 53, 5684-5695.

Clayton, J.D., 2018. Mesoscale models of interface mechanics in crystalline solids: a review. J. Mater. Sci. 53, 5515-5545.

Cui, Y., Liu, Z., Zhuang, Z., 2015. Quantitative investigations on dislocation based discrete-continuous model of crystal plasticity at submicron scale. Int. J. Plast. 69, 54-72.

Damadam, M., Shao, S., Ayoub, G., Zbib, H.M., 2018. Recent advances in modeling of interfaces and mechanical behavior of multilayer metallic/ceramic composites. J. Mater. Sci. 53, 5604-5617.

Dehm, G., Jaya, B.N., Raghavan, R., Kirchlechner, C., 2018. Overview on micro- and nanomechanical testing: New insights in interface plasticity and fracture at small length scales. Acta Mater. 142, 248-282.

Devincre, B., Hoc, T., Kubin, L., 2008. Dislocation Mean Free Paths and Strain Hardening of Crystals. Sci. 320, 1745.

Dodaran, M., Wang, J., Chen, Y., Meng, W.J., Shao, S., 2019. Energetic, structural and mechanical properties of terraced interfaces. Acta Mater. 171, 92-107.

Eisenlohr, P., Diehl, M., Lebensohn, R.A., Roters, F., 2013. A spectral method solution to crystal elasto-viscoplasticity at finite strains. Int. J. Plast. 46, 37-53.

Embury, J.D., Hirth, J.P., 1994. On dislocation storage and the mechanical response of fine scale microstructures. Acta Metall. Mater. 42, 2051-2056.

Eshelman, F.R., Smith, J.F., 1978. Single - crystal elastic constants of Al2Cu. J. Appl. Phys. 49, 3284-3288.

Friedman, L.H., Chrzan, D.C., 1998. Scaling Theory of the Hall-Petch Relation for Multilayers. Phys. Rev. Lett. 81, 2715-2718.

Hill, R., Rice, J.R., 1972. Constitutive analysis of elastic-plastic crystals at arbitrary strain. J. Mech. Phys. Solids 20, 401-413.

Hodapp, M., Anciaux, G., Molinari, J.F., Curtin, W.A., 2018. Coupled atomistic/discrete dislocation method in 3D Part II: Validation of the method. J. Mech. Phys. Solids 119, 1-19.

Huang, S., Huang, M., Li, Z., 2018. Effect of interfacial dislocation networks on the evolution of matrix dislocations in nickel-based superalloy. Int. J. Plast. 110, 1-18.

Ignat, M., Durand, F., 1976. Deformation lines on Al2Cu single crystals after creep in compression. Scripta Metall. 10, 623-626.

Kapp, M.W., Hohenwarter, A., Wurster, S., Yang, B., Pippan, R., 2016. Anisotropic deformation characteristics of an ultrafine- and nanolamellar pearlitic steel. Acta Mater. 106, 239-248.

Kim, J., Kang, K., Ryu, S., 2016. Characterization of the misfit dislocations at the ferrite/cementite interface in pearlitic steel: An atomistic simulation study. Int. J. Plast. 83, 302-312.

Lee, T.C., Robertson, I.M., Birnbaum, H.K., 1989. Prediction of slip transfer mechanisms across grain boundaries. Scripta Metall. 23, 799-803.

Lei, Q., Ramakrishnan, B.P., Wang, S., Wang, Y., Mazumder, J., Misra, A., 2017. Structural refinement and nanomechanical response of laser remelted Al-Al2Cu lamellar eutectic. Mater. Sci. Eng. A 706, 115-125.

LeSar, R., Capolungo, L., 2018. Advances in Discrete Dislocation Dynamics Simulations, Handbook of Materials Modeling, pp. 1-32.

Li, J.C.M., Liu, G.C.T., 1967. Circular dislocation pile-ups. Philos. Mag.: A J. Theor. Exp. Appl. Phys. 15, 1059-1063.

Li, L., Anderson, P.M., Lee, M.-G., Bitzek, E., Derlet, P., Swygenhoven, H.V., 2009. The stress–strain response of nanocrystalline metals: A quantized crystal plasticity approach. Acta Mater. 57, 812-822.

Li, N., Liu, X.-Y., 2018. mechanical behavior of metal/ceramic interfaces in nanolayered composites—experiments and modeling. J. Mater. Sci. 53, 5562-5583.

Li, N., Wang, H., Misra, A., Wang, J., 2014. In situ Nanoindentation Study of Plastic Co-deformation in Al-TiN Nanocomposites. Sci. Rep. 4, 6633.

Li, N., Wang, J., 2015. In-situ TEM Study of Dislocation-Interface Interactions, The Transmission Electron Microscope-Theory and Applications. IntechOpen.

Liang, T., Ashton, M., Choudhary, K., Zhang, D., Fonseca, A.F., Revard, B.C., Hennig, R.G., Phillpot, S.R., Sinnott, S.B., 2016. Properties of Ti/TiC Interfaces from Molecular Dynamics Simulations. J. Phys. Chem. C 120, 12530-12538.

Lin, P., Liu, Z., Zhuang, Z., 2016. Numerical study of the size-dependent deformation morphology in micropillar compressions by a dislocation-based crystal plasticity model. Int. J. Plast. 87, 32-47.

Liu, G., Gong, M., Xie, D., Wang, J., 2019. Structures and Mechanical Properties of Al-Al2Cu Interfaces. JOM.

Lu, L., Huang, C., Pi, W., Xiang, H., Gao, F., Fu, T., Peng, X., 2018. Molecular dynamics simulation of effects of interface imperfections and modulation periods on Cu/Ta multilayers. Comput. Mater. Sci. 143, 63-70.

Lu, X., Zhang, X., Shi, M., Roters, F., Kang, G., Raabe, D., 2019. Dislocation mechanism based size-dependent crystal plasticity modeling and simulation of gradient nano-grained copper. Int. J. Plast. 113, 52-73.

Mara, N.A., Li, N., Misra, A., Wang, J., 2016. Interface-driven plasticity in metal–ceramic nanolayered composites: direct validation of multiscale deformation modeling via in situ indentation in TEM. JOM 68, 143-150.

Maresca, F., Kouznetsova, V.G., Geers, M.G.D., Curtin, W.A., 2018. Contribution of austenite-martensite transformation to deformability of advanced high strength steels: From atomistic mechanisms to microstructural response. Acta Mater. 156, 463-478.

Mayer, C.R., Molina-Aladareguia, J., Chawla, N., 2016a. Three dimensional (3D) microstructure-based finite element modeling of Al-SiC nanolaminates using focused ion beam (FIB) tomography. Mater. Charact. 120, 369-376.

Mayer, C.R., Yang, L.W., Singh, S.S., Llorca, J., Molina-Aldareguia, J.M., Shen, Y.L., Chawla, N., 2016b. Anisotropy, size, and aspect ratio effects on micropillar compression of AlSiC nanolaminate composites. Acta Mater. 114, 25-32.

Mayeur, J.R., Beyerlein, I.J., Bronkhorst, C.A., Mourad, H.M., 2015. Incorporating interface affected zones into crystal plasticity. Int. J. Plast. 65, 206-225.

Misra, A., Hirth, J., Hoagland, R., 2005a. Length-scale-dependent deformation mechanisms in incoherent metallic multilayered composites. Acta Mater. 53, 4817-4824.

Misra, A., Hirth, J., Hoagland, R., Embury, J., Kung, H., 2004. Dislocation mechanisms and symmetric slip in rolled nano-scale metallic multilayers. Acta Mater. 52, 2387-2394.

Misra, A., Zhang, X., Hammon, D., Hoagland, R.G., 2005b. Work hardening in rolled nanolayered metallic composites. Acta Mater. 53, 221-226.

Pant, P., Schwarz, K.W., Baker, S.P., 2003. Dislocation interactions in thin FCC metal films. Acta Mater. 51, 3243-3258.

Park, T., Hector, L.G., Hu, X., Abu-Farha, F., Fellinger, M.R., Kim, H., Esmaeilpour, R., Pourboghrat, F., 2019. Crystal Plasticity Modeling of 3rd Generation Multi-phase AHSS with Martensitic Transformation. Int. J. Plast., https://doi.org/10.1016/j.ijplas.2019.03.010.

Peirce, D., Asaro, R.J., Needleman, A., 1982. An analysis of nonuniform and localized deformation in ductile single crystals. Acta Metall. 30, 1087-1119.

Raghavan, R., Wheeler, J.M., Esqué-de los Ojos, D., Thomas, K., Almandoz, E., Fuentes, G.G., Michler, J., 2015. Mechanical behavior of Cu/TiN multilayers at ambient and elevated temperatures: Stress-assisted diffusion of Cu. Mater. Sci. and Eng. A 620, 375-382.

Roters, F., Diehl, M., Shanthraj, P., Eisenlohr, P., Reuber, C., Wong, S.L., Maiti, T., Ebrahimi, A., Hochrainer, T., Fabritius, H.O., Nikolov, S., Friák, M., Fujita, N., Grilli, N., Janssens, K.G.F., Jia, N., Kok, P.J.J., Ma, D., Meier, F., Werner, E., Stricker, M., Weygand, D., Raabe, D., 2019. DAMASK – The Düsseldorf Advanced Material Simulation Kit for modeling multi-physics crystal plasticity, thermal, and damage phenomena from the single crystal up to the component scale. Comput. Mater. Sci. 158, 420-478.

Roters, F., Eisenlohr, P., Hantcherli, L., Tjahjanto, D.D., Bieler, T.R., Raabe, D., 2010. Overview of constitutive laws, kinematics, homogenization and multiscale methods in crystal plasticity finite-element modeling: Theory, experiments, applications. Acta Mater. 58, 1152-1211.

Segurado, J., Lebensohn, R.A., LLorca, J., 2018. Computational Homogenization of Polycrystals. arXiv preprint arXiv:1804.02538.

Shanthraj, P., Diehl, M., Eisenlohr, P., Roters, F., Raabe, D., 2018. Spectral Solvers for Crystal Plasticity and Multi-physics Simulations, in: Schmauder, S., Chen, C.-S., Chawla, K.K., Chawla, N., Chen, W., Kagawa, Y. (Eds.), Handbook of Mechanics of Materials. Springer Singapore, Singapore, pp. 1-25.

Shao, S., Akasheh, F., Wang, J., Liu, Y., 2018a. Alternative misfit dislocations pattern in semi-coherent FCC {100} interfaces. Acta Mater. 144, 177-186.

Shao, S., Misra, A., Huang, H., Wang, J., 2018b. Micro-scale modeling of interface-dominated mechanical behavior. J. Mater. Sci. 53, 5546-5561.

Shao, S., Wang, J., 2016. Relaxation, Structure, and Properties of Semicoherent Interfaces. JOM 68, 242-252.

Shao, S., Wang, J., Beyerlein, I.J., Misra, A., 2015. Glide dislocation nucleation from dislocation nodes at semi-coherent {111} Cu–Ni interfaces. Acta Mater. 98, 206-220.

Shao, S., Zhou, C., Misra, A., Wang, J., 2018c. Mesoscale Modeling of Dislocation-Interactions in Multilayered Materials, in: Andreoni, W., Yip, S. (Eds.), Handbook of Materials Modeling : Methods: Theory and Modeling. Springer International Publishing, Cham, pp. 1-30.

Tome, C., Canova, G.R., Kocks, U.F., Christodoulou, N., Jonas, J.J., 1984. The relation between macroscopic and microscopic strain hardening in F.C.C. polycrystals. Acta Metall. 32, 1637-1653.

Wang, J., Hoagland, R.G., Hirth, J.P., Misra, A., 2008a. Atomistic modeling of the interaction of glide dislocations with “weak” interfaces. Acta Mater. 56, 5685-5693.

Wang, J., Hoagland, R.G., Hirth, J.P., Misra, A., 2008b. Atomistic simulations of the shear strength and sliding mechanisms of copper–niobium interfaces. Acta Mater. 56, 3109-3119.

Wang, J., Misra, A., 2011. An overview of interface-dominated deformation mechanisms in metallic multilayers. Curr. Opin. Solid State Mater. Sci. 15, 20-28.

Wang, J., Misra, A., 2014. Strain hardening in nanolayered thin films. Curr. Opin. Solid State Mater. Sci. 18, 19-28.

Wang, J., Misra, A., Hoagland, R., Hirth, J., 2012. Slip transmission across fcc/bcc interfaces with varying interface shear strengths. Acta Mater. 60, 1503-1513.

Wang, J., Zhang, R., Zhou, C., Beyerlein, I.J., Misra, A., 2014a. Interface dislocation patterns and dislocation nucleation in face-centered-cubic and body-centered-cubic bicrystal interfaces. Int. J. Plast. 53, 40-55.

Wang, J., Zhou, C., Beyerlein, I.J., Shao, S., 2014b. Modeling Interface-Dominated Mechanical Behavior of Nanolayered Crystalline Composites. JOM 66, 102-113.

Wang, J., Zhou, Q., Shao, S., Misra, A., 2017. Strength and plasticity of nanolaminated materials. Mater. Res. Lett. 5, 1-19.

Wang, S.J., Liu, G., Wang, J., Misra, A., 2018a. Characteristic orientation relationships in nanoscale Al-Al2Cu Eutectic. Mater. Charact. 142, 170-178.

Wang, S.J., Liu, G., Xie, D.Y., Lei, Q., Ramakrishnan, B.P., Mazumder, J., Wang, J., Misra, A., 2018b. Plasticity of laser-processed nanoscale AlAl2Cu eutectic alloy. Acta Mater. 156, 52-63.

Werner, E., Prantl, W., 1990. Slip transfer across grain and phase boundaries. Acta Metall. Mater. 38, 533-537.

Xiong, L., Deng, Q., Tucker, G., McDowell, D.L., Chen, Y., 2012. A concurrent scheme for passing dislocations from atomistic to continuum domains. Acta Mater. 60, 899-913.

Xu, S., Xiong, L., Chen, Y., McDowell, D.L., 2017. Comparing EAM Potentials to Model Slip Transfer of Sequential Mixed Character Dislocations Across Two Symmetric Tilt Grain Boundaries in Ni. JOM 69, 814-821.

Yang, L.W., Mayer, C., Chawla, N., Llorca, J., Molina-Aldareguía, J.M., 2016. Deformation mechanisms of ultra-thin Al layers in Al/SiC nanolaminates as a function of thickness and temperature. Philos. Mag. 96, 3336-3355.

Yu, L., Xiao, X., Chen, L., Cheng, Y., Duan, H., 2018. A hierarchical theoretical model for mechanical properties of lath martensitic steels. Int. J. Plast. 111, 135-151.

Zbib, H.M., Diaz de la Rubia, T., 2002. A multiscale model of plasticity. Int. J. Plast. 18, 1133-1163.

Zeng, Y., Hunter, A., Beyerlein, I.J., Koslowski, M., 2016. A phase field dislocation dynamics model for a bicrystal interface system: An investigation into dislocation slip transmission across cube-on-cube interfaces. Int. J. Plast. 79, 293-313.

Zhang, H., Liu, J., Sui, D., Cui, Z., Fu, M.W., 2018. Study of microstructural grain and geometric size effects on plastic heterogeneities at grain-level by using crystal plasticity modeling with high-fidelity representative microstructures. Int. J. Plast. 100, 69-89.

Zhang, R.F., Wang, J., Beyerlein, I.J., Misra, A., Germann, T.C., 2012. Atomic-scale study of nucleation of dislocations from fcc–bcc interfaces. Acta Mater. 60, 2855-2865.

Zhang, X., Godfrey, A., Hansen, N., Huang, X., Liu, W., Liu, Q., 2010. Evolution of cementite morphology in pearlitic steel wire during wet wire drawing. Mater. Charact. 61, 65-72.

Zhou, Q., Wang, J., Misra, A., Huang, P., Wang, F., Xu, K., 2016a. Atomistic study of fundamental character and motion of dislocations in intermetallic Al2Cu. Int. J. Plast. 87, 100-113.

Zhou, Y., Yang, W., Hu, M., Yang, Z., 2016b. The typical manners of dynamic crack propagation along the metal/ceramics interfaces: A molecular dynamics study. Comput. Mater. Sci. 112, 27-33.

Figures Captions

Fig. 1. Schematic illustration of confined layer slip mechanism in multilayers. (a) Propagation of two dislocations glide in one layer. (b) Uniform distribution of two groups of dislocations (blue and red) at the interface.

Fig. 2. (a) Illustration of a two bilayers model with equal thickness h for A and B layers. Each layer is meshed into three elements, referred to as lower, middle and upper elements and denoted as i = 1, 2 and 3 respectively. (b) Computation strategy for ensuring identical plastic deformation and heterogeneous elastic deformation through one lamella. For one layer composed of three elements (i = 1, 2 and 3), it includes a self-consistent inner-level integration of kinematic quantities at fixed internal plastic state, and an outer-level integration of internal material state using the average stress in the three elements.

Fig. 3. (a, c) Illustration of a three dimensional periodic two bilayers Al-Al_2Cu lamellar structure model used in buckling simulation. (a) Initial configuration, and (c) Perturbated configuration after small amplitude sinusoidal perturbations applied to the initial geometry. Simple compression loading parallel to the lamellae (along x-axis) is applied to the perturbated configuration to simulate the buckling deformation of the layers. (b) Experimentally observed elastic bending of Al_2Cu lamellae in nanolayered Al-Al_2Cu after rolling parallel to lamellae, reproduced from (Wang et al., 2018b).

Fig. 4. Slip systems in upper α-Al and lower θ-Al_2Cu lamellae across the $(001)_\alpha \| (001)_\theta$ interface for compression strain is applied along (a) z-$[001]_\alpha \| [001]_\theta$ direction normal to interface and (b) $[110]_\alpha \| [2\bar{1}0]_\theta$ direction in the interface plane. The red and blue vectors on their corresponding slip planes are the activated slips in upper α-Al and lower θ-Al_2Cu respectively, and the vector numbers in Al are colored by their slip plane color.

Fig. 5. (a) Compressive stress-strain curves and (b) corresponding strain hardening rate of Al-Al_2Cu nanolayers with layer thickness of 86 nm under compression normal to $(001)_\alpha \parallel (001)_\theta$ interface measured in micro-pillar compression experiment and predicted by the CLS-CP models with increasing relative dislocation activities in Al over that in Al_2Cu layer, $r_a = \dot{\gamma}_0^{Al}/\dot{\gamma}_0^{Al2Cu}$, varying from 1 to 30 representing increasing plastic incompatibility between the two layers.

Fig. 6. Effects of heterogeneous elastic deformation through layer thickness on the deformation behavior of Al-Al_2Cu with layer thickness of 40 nm under compression along x-$[110]_\alpha \parallel [2\bar{1}0]_\theta$. (a) Stress-strain curves, (b-c) Distribution of Mises equivalent plastic strain γ_M^p and equivalent stress σ_M at a compression strain ε_{xx} = -7.78%. (d-f) Distribution of stress component σ_{xx} along z-direction in Al and Al_2Cu layers at x = 0.25 L_x, 0.375 L_x and 0.5 L_x at a compression strain ε_{xx} = -7.78%.

Fig. 7. Mechanical response of Al-Al_2Cu composites with lamellar spacing of 40 nm under compression strain applied along x-$[110]_\alpha \parallel [2\bar{1}0]_\theta$ direction predicted by the CLS-CP (r_a = 10, 1) and standard CP models adopting either nanolayer Al (CP-N) or bulk Al (CP-B) constitutive parameters. (a) Average true stress-true strain curves, (b) deflection δ normalized by the thickness h and (c) Mises equivalent plastic strain in Al layer averaged over all elements of Al layers. (d-e) Evolution of accumulated plastic strain on s-th slip system averaged in all elements of (d) Al and (e) Al_2Cu layers respectively. The magnitude of $\gamma^{(s)}$ in Al layer predicted by CP-N and CP-B models shown in (d) is one third of the actual magnitude. (f) The accumulated plastic strain on s-th slip system in the lower (i = 1), middle (i = 1) and upper (i = 3) elements in Al and their average.

Fig. 8. (a-c) Distribution of von Mises equivalent plastic strain γ_M^p in Al-Al_2Cu alloy at compression strain ε_{xx} = -7.78% predicted by CLS-CP, CP-N and CP-B models. (d-i) Distribution of γ_M^p along x direction. γ_M^p(i) with i = 1, 2, 3, refers to the γ_M^p in the lower, middle or upper element of Al (d-f) and Al_2Cu (g-i) layer. γ_M^p(a) refers to the averaged Mises equivalent plastic strain of the three elements through the layer thickness.

Fig. 9. Distribution of (a-c) von Mises equivalent stress σ_M in Al-Al_2Cu alloy at compression strain ε_{xx} = -7.78% predicted by CLS-CP and CP-N models. (d-g) Distribution of Cauchy stress component σ_{xx} along x direction. $\sigma_{xx}^i$with i = 1, 2, 3, refers to σ_{xx} in the lower, middle and upper

element of Al or Al_2Cu layer respectively, and σ_{xx}^{a} refers to the averaged σ_{xx} of the three elements through one layer.

Fig. 10. Variation of (a) plastic strain component $\gamma_{xx}^{p}(i)$ and (b-c) Cauchy stress component σ_{xx}^{i} in the three elements (i = 1, 2, 3) of Al layer and their averages (i = a) among the three elements at maximum bend position x = 0.25 L_x with increasing applied compressive strain ε_{xx}. γ_{xx}^{p} is the same plastic strain in the three elements of Al layer predicted by the CLS-CP model.

Fig. 11. Effects of the layer thickness on stress-strain curves under parallel compression along $[110]_\alpha \| [2\bar{1}0]_\theta$ direction predicted by the CLS-CP model.

Fig. 12. Effects of loading direction on the deformation behavior. (a) Stress-strain curves and (b-c) evolution of plastic strain on s-th slip systems in Al_2Cu (b) and Al (c) layers in response of compression normal to the $(001)_\alpha \| (001)_\theta$ interface and along three directions in $(001)_\alpha$ plane, which are $[110]_\alpha \| [2\bar{1}0]_\theta$, $+10°$ (hard) and $-10°$ (soft) clockwise deviating from $[110]_\alpha$ direction respectively.

Confined Layer Slip – Crystal Plasticity

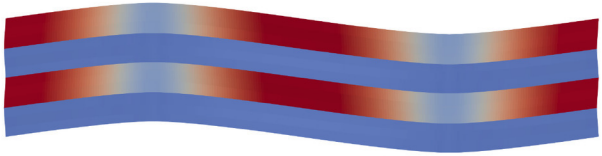

Constant plasticity through layer thickness

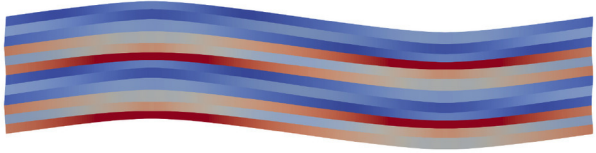

Heterogeneous elasticity through layer thickness